Geochemistry, Geophysics, Geosystems

RESEARCH ARTICLE
10.1029/2019GC008611

Key Points:
- Syn-eruptive transition from Hawaiian fountaining to transient ash explosions is marked by shallow magmatic degassing and crystallization
- Degassed, crystallized, and impermeable shallow magmatic layers can potentially form and burry vents with low eruptive activity
- Geophysical and geochemical monitoring evidenced a late arrival of a magma that pressurized the buried vent triggering ash explosions

Supporting Information:
- Supporting Information S1
- Table S1
- Table S2
- Table S3
- Table S4
- Table S5

Correspondence to:
S. Thivet,
simon.thivet@uca.fr

Citation:
Thivet, S., Gurioli, L., Di Muro, A., Derrien, A., Ferrazzini, V., Gouhier, M., et al. (2020). Evidences of plug pressurization enhancing magma fragmentation during the September 2016 basaltic eruption at Piton de la Fournaise (La Réunion Island, France). *Geochemistry, Geophysics, Geosystems*, *21*, e2019GC008611. https://doi.org/10.1029/2019GC008611

Received 7 AUG 2019
Accepted 27 DEC 2019
Accepted article online 22 JAN 2020

Evidences of Plug Pressurization Enhancing Magma Fragmentation During the September 2016 Basaltic Eruption at Piton de la Fournaise (La Réunion Island, France)

Simon Thivet[1], Lucia Gurioli[1], Andrea Di Muro[2], Allan Derrien[2], Valérie Ferrazzini[2], Mathieu Gouhier[1], Diego Coppola[3], Bo Galle[4], and Santiago Arellano[4]

[1]Laboratoire Magmas et Volcans, Université Clermont Auvergne - CNRS - IRD, OPGC, Campus Universitaire des Cézeaux, Aubière Cedex, France, [2]Observatoire Volcanologique du Piton de la Fournaise, Institut de Physique du Globe de Paris, Sorbonne Paris Cité, Univ. Paris Diderot, CNRS, F-97418, La Plaine des Cafres, La Réunion, Paris, France, [3]Dipartimento di Scienze della Terra, Università degli Studi di Torino, Via Valperga Caluso 3510125, Torino, Italy, [4]Department of Earth and Space Sciences, Chalmers University of Technology, Hörsalsvägen 11, 412 96 Gothenburg, Sweden

Abstract In September 2016, Piton de la Fournaise volcano, well known for its effusive and Hawaiian fountaining activity, produced, at the end of the eruption, an unusual phase of pulsating ash and bomb emission. Integration of geophysical data, with textural and petrological analysis of the samples, allowed us to constrain the main factors that controlled this sudden shift in activity, potentially dangerous for the tourist population that usually approach these "gentle" eruptive sites. Volcanic tremor, lava discharge rates, fountain heights, and SO_2 emission changed rapidly during the eruption. Grain size and componentry of the tephra beds evolved from unimodal all along the sequence to bimodal on the last day of the activity, reflecting the contribution of both Hawaiian fountaining at the main vent (Vent A) and transient explosive activity at the second vent (Vent B). Hawaiian fountaining produced highly vesicular and almost microlite-free tephra (golden pumice and fluidal scoria) while transient explosive activity emitted denser and crystal-rich tephra (sideromelane and tachylite scoria) sometimes mingled with vesicular fragments. Permeability measurements on lapilli and bomb-sized samples reveal that golden pumice and fluidal scoria were more gas-permeable than the sideromelane and tachylite ones, while textural and chemical analyses of the ash support the hypothesis that these sideromelane and tachylite components were inherited from the subsurface crystallization of the initial golden pumice and fluidal scoria components. We thus suggest that Vent B accumulated a plug of degassed, cooled, and low-permeable magma, which modulated overpressure pulses under the late input of ascending magma.

1. Introduction

Nowadays, active volcanoes are increasingly monitored and studied with a panel of multidisciplinary techniques. Focusing on basaltic volcanism and the associated volcanic hazards, ash-dominated explosions can potentially have large and unexpected impacts on the local populations and environments (e.g., Barsotti et al., 2010; Brown et al., 2017; Scollo et al., 2013). Even if these ash and bomb explosions can be relatively small and mild, they can pose a threat to the tourist population that usually approach these "gentle" eruptive sites (e.g., at Etna, Hawaii, Stromboli, Piton de La Fournaise, Masaya; see also Blong, 1984, 1996; Papale 2017; Morin et al., 2016). Thus, it is critical to characterize, quantify, and understand what control the transition from mild to more violent eruptive phases (e.g., Houghton et al., 2004; Sable et al., 2006; Andronico et al., 2009; Di Traglia et al., 2009; Cimarelli et al., 2010; Corsaro et al. 2017) and what control the magmatic processes occurring before and during an explosive event (e.g., Arzilli et al., 2015, Arzilli, La Spina, et al., 2019; Di Muro et al., 2014, 2015, 2016; Edwards et al., 2018; Gurioli et al., 2018; Villemant et al., 2009). Many studies proved that textural quantification, in terms of vesicle and crystal contents and size distributions of basaltic erupted products like bombs (e.g., Gurioli et al., 2014; Gurioli et al., 2018; Jones et al., 2018; Leduc et al., 2015; Rosseel et al. 2006), lapilli (e.g., Carey et al., 2012; Costantini et al., 2010; Gurioli et al., 2018; Holt et al., 2019; Houghton & Wilson, 1989; Lautze & Houghton, 2005; Marsh, 1988; Mangan & Cashman, 1996; Parcheta et al., 2013; Polacci et al., 2006, 2009; Sparks, 1978; Stovall et al., 2011;

Toramaru 1989; Walker & Croasdale, 1971), and more recently ash (e.g., Cannata et al., 2019; Cioni et al., 2008, 2014; D'Oriano et al., 2011, 2014; Lautze et al., 2013; Liu et al., 2015; Porritt et al., 2012; Taddeucci et al., 2002, 2004) are fundamental to achieve this goal. Since the 2000s, new approaches have been developed by combining textural measurements on basaltic tephra with field data (e.g., Andronico et al., 2014; Edwards & Pioli, 2019; Romero et al., 2018), petrological and geochemical analysis (e.g., Bai et al., 2011; Di Muro et al., 2014, 2015; Gurioli et al., 2018; Pioli et al., 2014; Polacci et al., 2006; Pompilio et al., 2017; Taddeucci et al., 2002, 2004), and geophysical insights (e.g., Andronico et al., 2008, 2013, 2014; Burton et al., 2007; Colò et al., 2010; Gurioli et al., 2008, 2013, 2014; Leduc et al., 2015; Miwa et al., 2009; Miwa & Toramaru, 2013; Patrick et al., 2007; Pistolesi et al., 2011; Polacci et al., 2009). Several of these studies have already shown that relative proportions between low-viscous (crystal-poor), high-viscous (crystal-rich), and volatile-poor and volatile-rich magmas within different levels of the magmatic conduits can potentially modulate the transition between Hawaiian/Strombolian and ash-dominated activities (Pompilio et al., 2017). The presence of debris within the superficial conduits (Patrick et al., 2007), the abundance of recycled materials (D'Oriano et al., 2014), or the presence of external fluids within the magmatic systems (Dellino et al., 2012) are also invoked for the origin of ash emissions. Following these approaches, we focused on the main factors that control the shift in activity from Hawaiian fountaining events to transient bomb and ash explosions during the September 2016 eruption at Piton de la Fournaise (PdF) volcano (La Réunion Island, France).

2. Geological Setting

PdF is one of the most active basaltic volcanoes on Earth (Peltier et al., 2018; Staudacher et al., 2016). On this volcano, investigations on prehistoric and historic deposits show that large volume explosive events can occur inside or outside the Enclos Fouqué caldera (e.g., Michon et al., 2013; Morandi et al., 2016; Ort et al., 2016), which is the most recent and main caldera of the volcano (Figure 1). More recent activity has also been well documented by Staudacher et al. (2016) and Peltier et al. (2018) especially between 1998 and 2013. This period was relatively active with an emitted magma volume of 32.6×10^6 m^3 per year on average. Since 1998, all the eruptions occurred within the Enclos Fouqué caldera, with variable durations (hours to months) and variable output rates (Roult et al., 2012; Coppola et al., 2017). These eruptions were mostly typical basaltic fissure eruptions with a few exceptions like the summit ash emission linked with the collapse of the Dolomieu summit caldera (Figure 1) during the April 2007 eruption (e.g., Michon et al., 2013; Peltier et al., 2009; Staudacher et al., 2009, 2016), which involved more magma than any other eruption at PdF since at least 200 years. Since, the eruptive regime at PdF has been mainly effusive, coupled with more or less intense Hawaiian-style and weak Strombolian-style activity (e.g., Gurioli et al., 2018; Harris et al., 2017; Peltier et al., 2018). Weak Strombolian-style activity at PdF is mainly characterized by short and sporadic bubble bursts that only form coarse lapilli, bombs and spatters with scarce ash emission (DynVolc 2017; Gurioli et al., 2018), while Hawaiian-style fragmentation is characterized by moderate sustained lava fountains, following the classification of Houghton et al. (2016), and usually produce lapilli and coarse ash sometimes with Pele's hairs (e.g., Di Muro et al., 2014, 2015; Gurioli et al., 2018; Villemant et al., 2009).

More recently, the 11–18 September 2016 eruption produced a different and unexpected behavior. While typical Hawaiian fountaining dominated the entire eruption, ash and bombs were produced the last day of the eruptive activity. Although this ash formation has been relatively weak compare to big explosive and plume forming events (e.g., the more violent Strombolian events of 1759, 1791, 1860, and 1961 eruptions; Michon et al., 2013), this kind of discreet ash plumes are very unusual in the recent activity of PdF. Similarly to the Hibert et al. (2015) approach to the January 2010 eruption at PdF (that was without ash emissions), the purpose of this study was to gather and organize all the useful data sets to trace the complex degassing and fragmentation history of the September 2016 eruption and, above all, understand the formation of this uncommon ash, which represent an unexpected hazard that could potentially occur during the next eruptions at PdF and other basaltic systems.

3. Methods

3.1. Field Observations, Samplings, and Monitoring Networks

The September 2016 eruption lasted 7 days, from the 11th to 18th. Field sampling was jointly realized by the Observatoire Volcanologique du Piton de la Fournaise (OVPF, La Réunion, France) and by the DynVolc

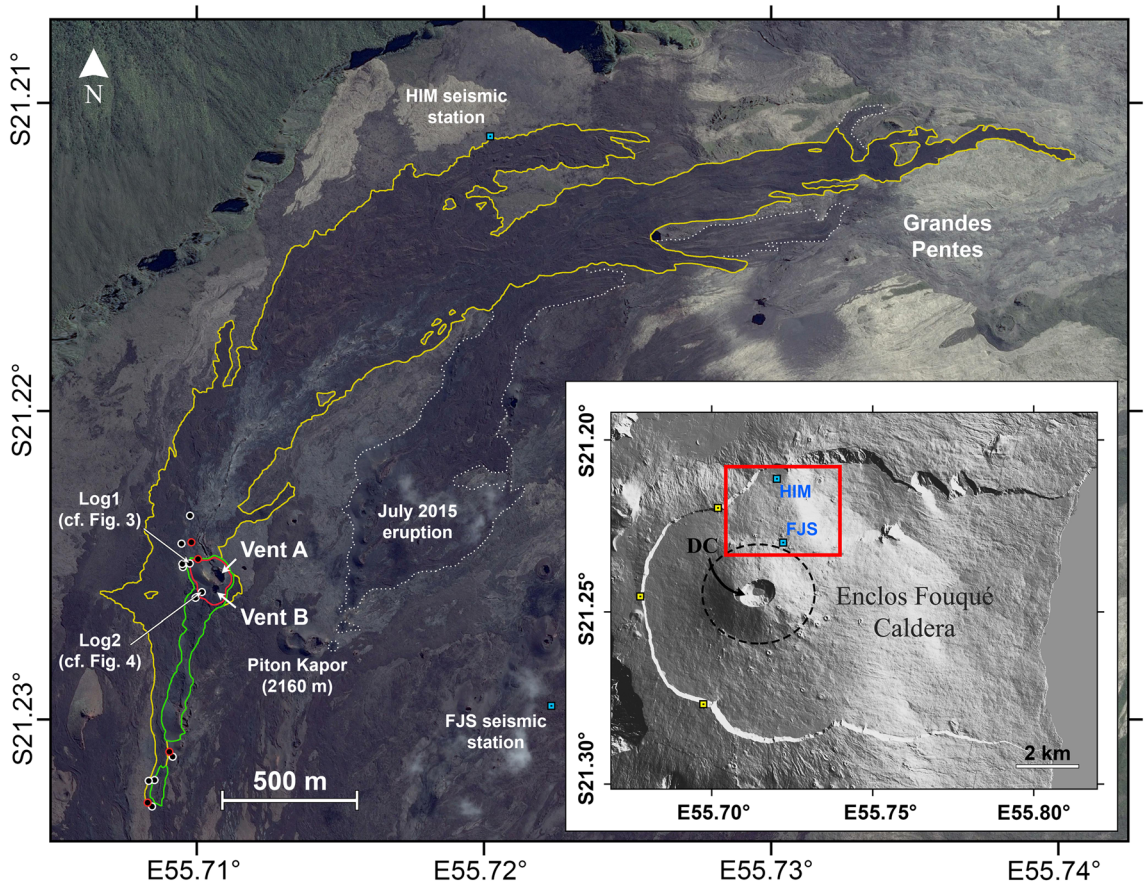

Figure 1. Map of the September 2016 eruption with associated DEM of PdF. DC: Dolomieu caldera. The black dashed line represents the central cone of PdF. Blue and yellow squares are the location of the seismic and NOVAC stations, respectively. White and red dots represent the different tephra and lava sampling sites, respectively. The yellow, green, and red lines represent respectively the outline of the lava flows, the eruptive fissure system, and main active cone edifice with Vents A and B.

teams (from the Observatoire de Physique du Globe de Clermont-Ferrand and from the Laboratoire Magmas et Volcans). Since the first day of activity, several samples were collected during the eruption, especially on the southern and upper tip of the fracture system. Other samplings were done on 16 September, still during the volcanic activity (Table S1 in the supporting information). Syn-eruptive tephra sampling was performed by hand, and a galvanized steel pipe was used to sample the molten lava near the source of emission. Then, these samples were gently quenched in water. Other samples were collected a few days after the end of eruption to be able to access very proximal and strategic deposits in order to reconstruct the entire sequence of the eruption (Figure 1). The purpose of the sampling was to identify all the different components of the emitted tephra during the eruption, to quantify their respective proportions, while preserving the most primitive signature of the juvenile magma (Gurioli et al., 2015; Gurioli et al., 2018; Harris et al., 2017). These different samples were carefully numbered, sorted (Table S1), and sent to the Laboratoire Magmas et Volcans, in Clermont-Ferrand (France), to be analyzed in terms of textural, petrological, and geochemical analyses. The raw data used in this study are available in the DynVolc database (2017) as well as in the supporting information of this article.

Data from the field monitoring network of the OVPF were compiled to constrain the volcano dynamics before and during the eruption. The evolution of all the monitoring measurements listed hereafter (volcanic tremor, lava discharge rate, ash emission, and SO_2 flux) could be compared in order to quantify the evolution of the eruptive dynamics (Hibert et al., 2015). Ground-based (webcam situated 1,100 m from the active vents and cameras) and aerial photos (drone) taken during the eruption, permitted to continuously follow the eruptive activity (depending on the weather conditions). The volcanic tremor is usually generated by the movement of magmatic fluids, and this signal is continuously recorded by the seismic stations of the

OVPF. In this study, tremor data from Crater Himiltrude (HIM) and Piton Faujas (FJS) seismic stations (broad-band three-components stations; Battaglia et al., 2016; white squares on Figure 1) are filtered on five different frequency bands (from 0.5 to 32 Hz). Pre- and syn-eruptive deformation was monitored on three different Global Navigation Satellite System baselines (Peltier et al., 2018). In order to quantify the lava discharge rate of the eruption, we combined in this study two different data sets from two near real-time remote sensing systems: (i) the HOTVOLC observing system (Gouhier et al., 2012, 2016), using data from the Spinning Enhanced Visible and InfraRed (IR) Imager, onboard the geostationary platform Meteosat (MSG-SEVIRI) and (ii) the MIROVA observing system (Coppola et al., 2009, 2016, 2017; Coppola & Cigolini, 2013), using the sun-synchronous orbit of two satellites (Terra and Aqua), which embed the Moderate Resolution Imaging Spectroradiometers. From the HOTVOLC system, we were able to collect thermal data every 15 min and to generate high temporal resolution time series of the lava Volume Flow Rate, obtained from IR satellite data. Also, the MIROVA system collected thermal data every 6 hr to deduce a time series of the Time-Averaged Discharge Rate. Hereafter, Volume Flow Rate and Time-Averaged Discharge Rate are described as lava flux. From webcam images analysis (one image every 2 min), HOTVOLC-derived lava flux data set was filtered and discarded in case of significant low-altitude cloud cover, which can possibly disturb these space-based IR measurements. In order to be compared with MIROVA-derived lava flux, we applied a moving average on seven points (~2 hr) for the entire HOTVOLC-derived lava flux data set. Using the HOTVOLC system, we were also able to qualitatively monitor the presence or the absence of both ash plumes and SO_2 emission (Guéhenneux et al., 2015). In parallel, SO_2 flux measurements were quantitatively estimated by the Network for Observation of Volcanic and Atmospheric Change (Galle et al., 2010), based on three ground-based ultraviolet absorption spectroscopy station arranged around the Enclos Fouqué caldera (yellow squares on Figure 1). These measurements, taken with a typical rate of one gas flux value every 10 min, led to a single averaged SO_2 flux value each day during the monitoring period, as well as to daily statistics of gas plume direction and altitude.

3.2. Grain Size and Componentry

Grain size analysis were performed following the procedure of Gurioli et al. (2018), on samples within two log sections (eight different layers in total) representing the entire sequence emplaced during the September 2016 eruption. Samples were dried in the oven at 90 °C during a minimum duration of 24 hr. To avoid bias in the grain size data, sieving was realized manually because the main part of the deposit was highly vesicular and fragile. Componentry was carried out in two steps. First, it follows the nomenclature of White and Houghton (2006), to distinguish juvenile, nonjuvenile, and composite clasts. Then, all these clasts were classified into different juvenile components depending on their colors, surface, and shapes (e.g., Gurioli et al., 2018; Pompilio et al., 2017; Stovall et al., 2012) within the bomb- and lapilli-size fractions as well as the coarse ash particles (>500 μm in diameter).

3.3. Bulk Texture Analysis (Porosity, Helium Connectivity, and Air Permeability)

Bulk texture analysis were performed on a selection of different clasts. Envelope density and helium vesicle connectivity were measured on 108 samples from the September 2016 eruption, following the procedure detailed on the supplementary material (Thivet et al. submitted). Density measurements were realized using the Micromeritics Geopyc 1360 envelope density analyzer, and both helium vesicle connectivity and Dense Rock Equivalent measurements were performed using the Micromeritics Accupyc 1340 Helium pycnometer (Colombier, Wadsworth, et al., 2017; Formenti & Druitt, 2003; Kawabata et al., 2015). Density measurements allow us to calculate porosity of each pyroclasts, while helium vesicle connectivity measures the percentage of connected and isolated vesicles within each sample.

Ash density measurements were performed using water pycnometry following the procedure of Eychenne and Le Pennec (2012). Three different density measurements were carried out on each ash component. Ash componentry was first determined using basic macroscopic observations with binoculars while Scanning Electron Microscope (SEM, JEOL JSM-5910 LV, acceleration voltage of 15 kV) was used to acquire Back-Scattered Electron images on the different ash components. The grain size used for the water pycnometry was between 0.5 ϕ (710 μm) and 1 ϕ (500 μm) for all the components. A balance (precision of 10^{-3} g) was used, as well as high-precision pycnometers and distilled water. Envelope density of each ash component can be confidently determined supposing that the water does not enter the sample pores due to the relatively high water surface tension. The particles were weighed after each measurement, to confirm that the water did

not enter. At least 100 ash particles of the same component were used for each measurement. Thus, the calculated density and porosity value is the average of all the ash particles of that size, measured for each component.

Air permeability measurements were carried out on 64 samples (of known density and helium vesicle connectivity values) from different eruptions of PdF, 21 of which belong to the September 2016 eruption. The others are from recent Hawaiian/Strombolian-style activities between June 2014 and January 2017 (DynVolc 2017) and also from historical and intense activities of Piton Chisny black tephra fall (Hawaiian fountaining activity; Morandi et al., 2016; Principe et al., 2016; Colombier, Wadsworth, et al., 2017) and from the 1860 eruption (phreatomagmatic activity; Michon et al., 2013). This large range of samples from different eruptive dynamics allowed us to compare the permeability characteristics of different type of pyroclasts, both within the September 2016 eruption and with a larger set of samples. Following the procedure of Colombier, Gurioli, et al. (2017) and Gurioli et al. (2018), the clasts were cut into rectangular prisms (to know precise sample cross-sectional area that is required to calculate the permeability) and dried, before being imperviously wrapped with laboratory parafilm. The samples were then coated with resin. Then sample extremities were cut again to ensure to be resin-free and allow the airflow to pass through the sample. Some of the samples were destroyed during the preparation, which was sometimes difficult to perform due to the fragility of the samples. The prepared samples were then placed within the sample holder of the home-made permeameter following the instrumental processing of Takeuchi et al. (2008). The detailed characteristics of the permeameter are shown in the supporting information of this paper (Figure S1). The permeameter has a large broad measurements range, which allows to measure the permeability from 10^{-17} to 10^{-9} m^2. Two different flow meters of different measurement ranges (0–500 and 0–16,000 ml min^{-1}) as well as a differential pressure meter (0–200,000 Pa) are used to measure the airflow and the pressure drop across the sample, in order to solve the Forchheimer equation and deduce the Darcian (viscous) permeability k_1 of the measured samples (Bai et al., 2010; Rust & Cashman, 2004).

3.4. Ash Morphology

For each ash component, the method developed by Leibrandt and Le Pennec (2015) was used to characterize their projected 2-D morphology. Optimized morphometry of volcanic ash can yields crucial information on fragmentation processes during explosive activity (e.g., Büttner et al., 1999; Dellino et al., 2012; Heiken, 1974; Lautze et al., 2012; Liu et al., 2015; Maria & Carey, 2007; Nurfiani & Bouvet de Maisonneuve, 2018; Riley et al., 2003; Schmith et al., 2017; Sheridan & Marshall, 1983; Taddeucci et al., 2002; Wohletz, 1983). Several series of Apparent Projected Shape of Ash (APASH) on a very high number of ash particles were carried out using the automatized morpho-grainsizer Morphologi G3 of Malvern, able to disperse the ash sample on a glass slide and measure both the size and the morphology of the particles. APASH can be represented by roughness parameters as the solidity (SLD) and the convexity (CVX), which represent morphological (particle scale) and textural (smaller scale) roughness of the particles respectively (Liu et al., 2015), as well as shape parameters like the aspect ratio (AR). These three parameters were used to compare the different morphology characteristics of the ash and are defined using simple relations summarized by Leibrandt and Le Pennec (2015): $SLD = A/A_{CH}$, $CVX = P_{CH}/P$ and $AR = W_b/L_b$ where A is the particle area (μm^2), A_{CH} is the convex-hull area that is the area contain in the convex-hull perimeter (μm^2), P is the particle perimeter (μm), P_{CH} the convex-hull perimeter that is the smallest convex polygon that contains all the pixels of the particle (μm), and W_b the minor axis and L_b the major axis of the particle. SLD, CVX, and AR values are thus dimensionless values between 0 and 1. This way, we measured the ash particles morphologies on the 0.5–1 ϕ (710–500 μm) grainsize fraction for each ash component. The raw data were filtered in case of artificial particle agglomerates. Statistical analysis on these morphology data were also performed using boxplot representation.

3.5. Chemical Analysis

Chemical analyses were performed following the same procedure adapted by Gurioli et al. (2018). Glass and crystals in situ measurements for major elements were carried out on the ash fraction using a Cameca SX100 electron microprobe, with a 15 kV acceleration voltage and a focused spot size (1 μm) for crystals and a spot diameter of 10 μm for the glass. Bulk rock compositions on the September 2016 products were performed by ICP-AES (Horiba Jobin-Yvon Ultima C spectrometer) analysis, both on coarse (bombs and lapilli) and fine (ash) samples. All these analysis and associated errors are provided in the supporting information.

3.6. Microtexture Analysis

Petrographic observations and microtexture analysis were performed using optical microscope and SEM imagery (BSE) on selected bomb and ash samples. Vesicle size distribution (VSD), vesicle number density (N_V), and vesicle to melt ratio (V_G/V_L) were measured following the Shea et al. (2010) procedures. In these calculations, the volume of melt is considered as microphenocryst-free and bubble-free. Crystal size distribution (CSD) and crystal number density (N_C) were measured following the Higgins (2000, 2002, 2006) approach. The procedures are detailed in the supporting information (Thivet et al. submitted). For these microtextural quantification, 15 ash particles (0.5–1 ϕ grainsize fraction) were used on average for each component in order to statistically acquire enough textural data (based on the vesicle and crystal quantity to count). Both for vesicles and crystals, the minimum object size measured was 2 pixels (equivalent to 3 μm for the most common used magnification 90x with the SEM). Based on our analyses and using the crystals shape database of Morgan and Jerram (2006), average crystal habits (x:y:z) for plagioclase (plg), clinopyroxene (cpx), olivine (ol), and oxides (ox) are, respectively, 1:3.2:10, 1:1.3:2, 1:1.4:1.4, and 1:1:1.

4. Results

4.1. The September 2016 Eruption

4.1.1. Eruptive Precursors

The September 2016 eruption is the seventh eruption at PdF since its reactivation in 2014 (after more than 3 years of rest; Gurioli et al., 2018) and the second of 2016 (after the May 2016 eruption). Midterm precursors were represented by a short seismic crisis associated with slight ground inflation around 50 days before the eruption (Peltier et al., 2018). Then, after 1 month of quiescence with no significant ground deformation, SO_2 emissions from the summit craters began to slightly increase from 27 August. Shallow seismic activity located below the central cone suddenly increase on 10 September (20 volcano-tectonics earthquakes, VT), just few hours before the beginning of the eruption. On the 11th, an intense seismic swarm (489 VT) started at 3:35 (all time cited in this paper are in UTC, LT = UTC+4 hr), and the eruption began at 4:35, which was confirmed by the thermal anomaly detected by the HOTVOLC system at 04:45. During the eruptive activity, which ended shortly after midnight of 18 September, summit, basal, and distant GPS baselines did not record significant ground deformation.

4.1.2. Volcanic Tremor, Lava Flux, and SO_2 Emissions

High-frequency (4–8 and 8–32 Hz) and low-frequency (0.5–1 Hz) bands of the volcanic tremor had relatively low intensities during the eruption, except at the beginning of the eruption (when the signal was relatively high) and for some short-lived anomalies. The anomalies in the very high-frequency (8–32 Hz) band reflected very local disturbance near the FJS seismic station when the lava flow path was very close to the station (Figure 1). The intermediate-frequency (1–2 and 2–4 Hz) bands had relatively high intensities that broadly correlate with the evolution of the eruption intensity, the lava flux (both from HOTVOLC and MIROVA data sets), and the SO_2 emissions (Figure 2). The tremor (2–4 Hz) level reached its highest level very soon at the beginning of the eruption, which was synchronous to the opening of several vents aligned on a 900 m long fissure, where sustained lava fountains (height of about 40 m) were observed. The associated lava flux (between 30 and 50 $m^3\ s^{-1}$) and SO_2 emissions (2,500 tons day^{-1}) were also the highest recorded within the eruption. Then, the volcanic tremor, lava flux (around 10 $m^3\ s^{-1}$), and SO2 emissions (down to 200 tons day^{-1}) rapidly decreased and slightly fluctuated at low levels until 13 September, at 12:00. This decrease in intensity was linked with the progressive closure of the southern part of the fissure, with still active Hawaiian fountaining within the Northern tip of the fissure (12 September). From the 13th, only two closely spaced vents remained active until the end of the eruption. We named them Vents A and B (Figure 1). Between the 13th, at 12:00, and the 16th, at 00:00, the tremor slightly increased and reached intermediate and stable levels, with peaks reflecting short-lived (few minutes) but intense fountaining activity in the main cone A (up to four times the average fountain height equivalent to a maximum of 150 m high, e.g., on the 14th, at 18:00, and on the 15th, at 12:00). These short-lived but relatively intense phases were immediately followed by sudden edifice collapses coupled with lava overflow, which briefly increased the IR signal recorded by the HOTVOLC system (around 25 $m^3\ s^{-1}$). During the whole day of the 16th, we observed a slight decrease in the intensity of the tremor, without significant changes of the lava flux and SO_2 emissions. In the meantime, visual observations confirmed that lava fountains remained active on Vent A while only a very slight degassing was observed on Vent B. Then, a progressive increase in the tremor intensity was

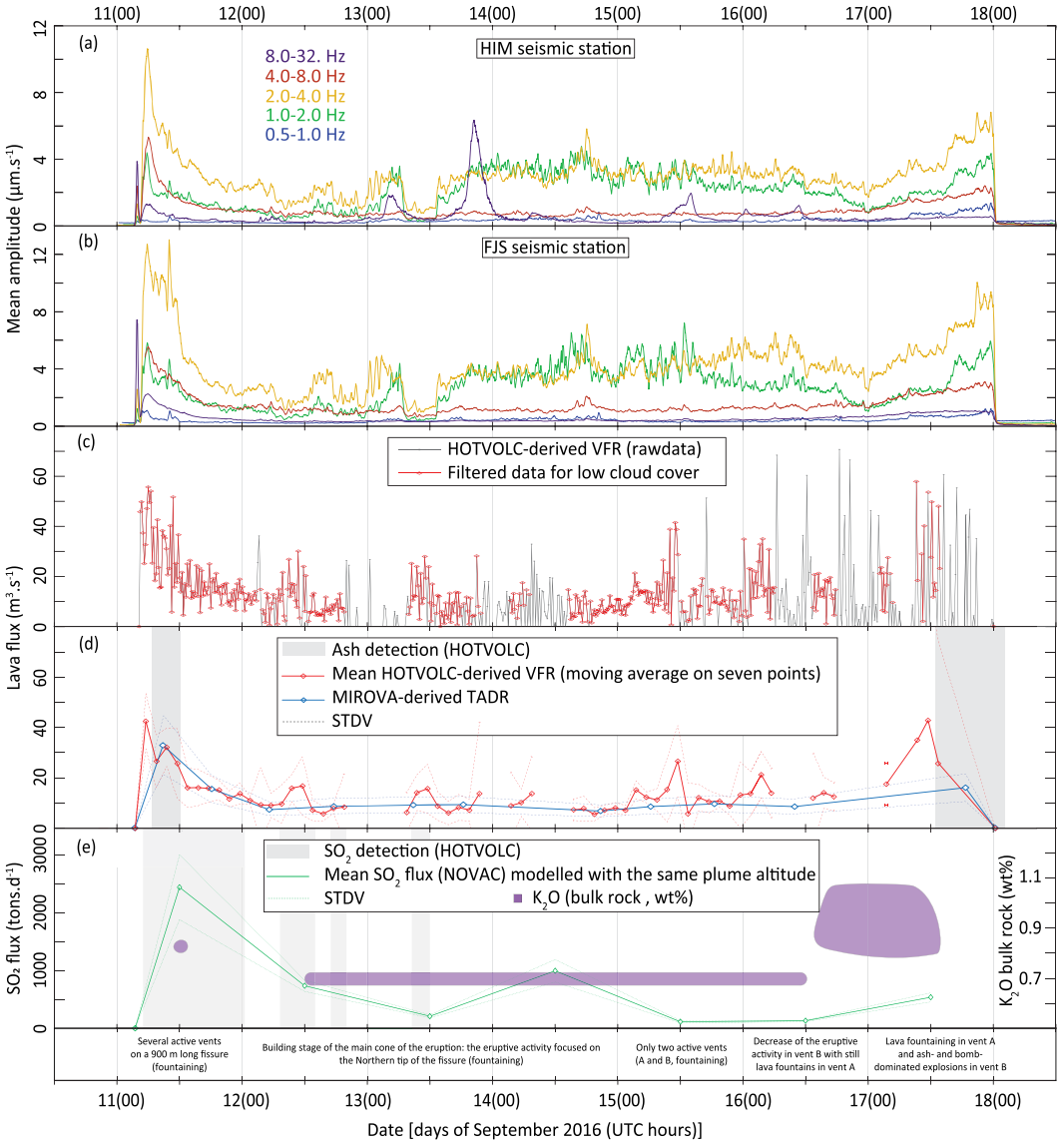

Figure 2. (a and b) Evolution of the volcanic tremor measured by the HIM and FJS seismic stations respectively. (c and d) The evolution of the lava fluxes by the HOTVOLC system (raw data, filtered data, and average) and the MIROVA system. Periods with ash detected by HOTVOLC are displayed in gray areas. (e) Evolution of the SO_2 flux measured by the NOVAC stations. Periods with SO_2 detected by HOTVOLC are displayed in gray areas.

observed during the whole day of the 17th, which correlated with the lava flux (between 20 and 40 $m^3\ s^{-1}$) and SO_2 emissions (around 600 tons day^{-1}) increase. This changes in terms of the geophysical signals were also visible on the field as the eruptive activity within Vent B reactivated, which was characterized by bomb- and ash-dominated transient explosions, while Hawaiian fountaining (fountain heights around 30 m) was still active within Vent A. The eruption suddenly stopped on 18 September around midnight.

The cumulative volume estimated with HOTVOLC data is $6.5 \times 10^6\ m^3$, while estimated cumulative volume with the MIROVA data is $6.1 \times 10^6\ m^3$. These estimations are relatively coherent with the total erupted volume of 5.9×10^6 and $6.8 \times 10^6\ m^3$ calculated by photogrammetry (Peltier et al., 2018). This total emitted volume and the duration of the eruption can be considered as intermediate values regarding the recent eruptions at PdF (Peltier et al., 2018). The associated lava flow expanded to the N-NE until the Grandes Pentes area and cover a small part of the July 2015 lava flow (Figure 1). Note that the ash-dominated events detected by the HOTVOLC system are also displayed in gray areas in Figure 2d and correspond to the beginning and

end of the eruption. Ash detected at the beginning may correspond to typical fountain-fed plumes during the initial high magmatic flux. Ash plumes during the last day of activity were well observed by satellite and ground-based field observations. Actually, these ash plumes and bomb emission were produced by sporadic pulses, well observed every 10–20 s on average. The maximum plume height was estimated around 300–400 m above the source and was slightly higher than the northern caldera wall of the Enclos Fouqué caldera. Thus, some of the eruptive products probably impacted the tourist and local population situated outside the caldera.

4.1.3. Stratigraphy and Componentry

The detailed sampling of the pyroclastic deposits located near the main active cone (delimited in red in Figure 1) allowed us to identify the different layers emplaced during the entire eruption. Log 1 corresponds to a sampling site situated 100 m to the NE from Vent A (Figures 1 and 3). Log 1 encompasses the whole sequence of Vent A activity, active during the entire eruption (Hawaiian fountaining), and it also includes the ash deposit from Vent B (Figure 4) that was emplaced on 17 September (based on field observations and wind direction). The first 40 cm of Log 1 sequence are formed by a clast-supported, reversely graded bed of golden pumice and scarce fluidal fragments (Figure 5a; following Gurioli et al., 2018, nomenclature). The particle size distributions (PSDs) of this bed (base, middle, and top; Histograms 1 to 3 in Figure 3) are asymmetric and are mostly comprised between lapilli and coarse ash, with a mode between −3 and −2.5 ϕ. Histograms 1 and 2 are bimodal with a coarse mode (Histograms 1 and 2) between −5.5 and −4 ϕ (bomb). The reverse gradation is marked by an increase in the amount of bombs up to 15 cm in diameter. Big bombs were not sampled due to their large size, and thus, they do not appear in the PSDs. This first sequence is overlain by a clast-supported, 30 cm thick, normally graded bed with similar components and PSD to that of the previous beds (Histogram 4, Figure 3). All these pyroclasts were deposited during the first 6 days of the eruption (from 11 to 16 September), forming a 70 cm thick bed. During the seventh and last day of the activity, the previous sequence was overlain by two 5 cm thick finer beds (Histograms 5 and 6, Figure 3). The PSDs of the two ash-rich beds are bimodal and comprises a first coarse-grained population, with a mode between −3 and −2.5 ϕ (for Layer 5, Figure 3) and between −4 and −3.5 ϕ (for Layer 6, Figure 3), composed by golden pumice and scarce fluidal scoria, emitted by Vent A. The fine-grained population, is formed by dense and opaque particles (tachylite texture, Figure 5b) with scarce transitional particles (sideromelane texture, Figure 5b), emplaced by Vent B activity. The PSD of this fine grained population is symmetric and comprised between −2 and 4.5 ϕ, the mode being systematically between 0.5 and 1 ϕ (Histograms 5 and 6, Figure 4). These relatively fine deposits are overlain by scattered golden pumice, fluidal scoria, and rare tachylite bombs (Figure 5a), coming from the very last activity of both vents.

Log 2 (Figure 4) is situated 70 m WSW from Vent B and is representative (still based on field observations and wind direction) of the proximal deposits from Vent B during the last day of the eruption. At this site, deposits are 50 cm thick (two bulk samples were collected, at the base and at the top of the deposits) and are composed of coarse golden pumice, fluidal, sideromelane, tachylite, and scarce mingled scoria fragments (Figure 5a). In both sampled beds (Histograms 7 and 8 in Figure 4), PSDs are unimodal, very asymmetric, skewed to relatively coarse grainsize (because of the proximity of the sampling to the vent) with a mode between −5 and −4.5 ϕ and between −4 and −3.5 ϕ for Layers 8 and 9, respectively. In comparison to Layers 5, 6, and 7 (Log 1, Figure 3), the fine fraction of these proximal deposit is mainly composed of sideromelane ash associated with scarce tachylite ash. Tachylite ash were mainly transported by the transient ash plumes and were deposited further North, within Log 1 (Figure 3). Sideromelane ash particles are abundant in the proximal sampling site of Vent B (Log 2) and have a metallic aspect because of the condensate deposition (Vlastélic et al., 2016, Figure 5b). Sideromelane ash particles are scarce in distal sampling site (Log 1) and have a glassy aspect without condensate deposition (Figure 5b). Note that, during the last day of the eruption, Vent B activity oscillated between (i) slight degassing around the crater rim to (ii) transient emissions of incandescent (golden and sideromelane material) as well as dark and opaque (tachylite material) bombs, and (iii) transient emission of dark ash within discrete plumes (mainly tachylite ash). These tachylite ash plumes seemed to be emitted from the crater boundaries while the bombs were emitted during larger explosions from the entire surface of the crater.

Based on their macroscopic characteristics, different components have been identified in the pyroclastic deposits, both during the syn-eruptive sampling and during the laboratory analysis (Figure 5). All the emitted products were juvenile. The Hawaiian fountaining produced only (i) golden pumice and scarce fluidal scoria

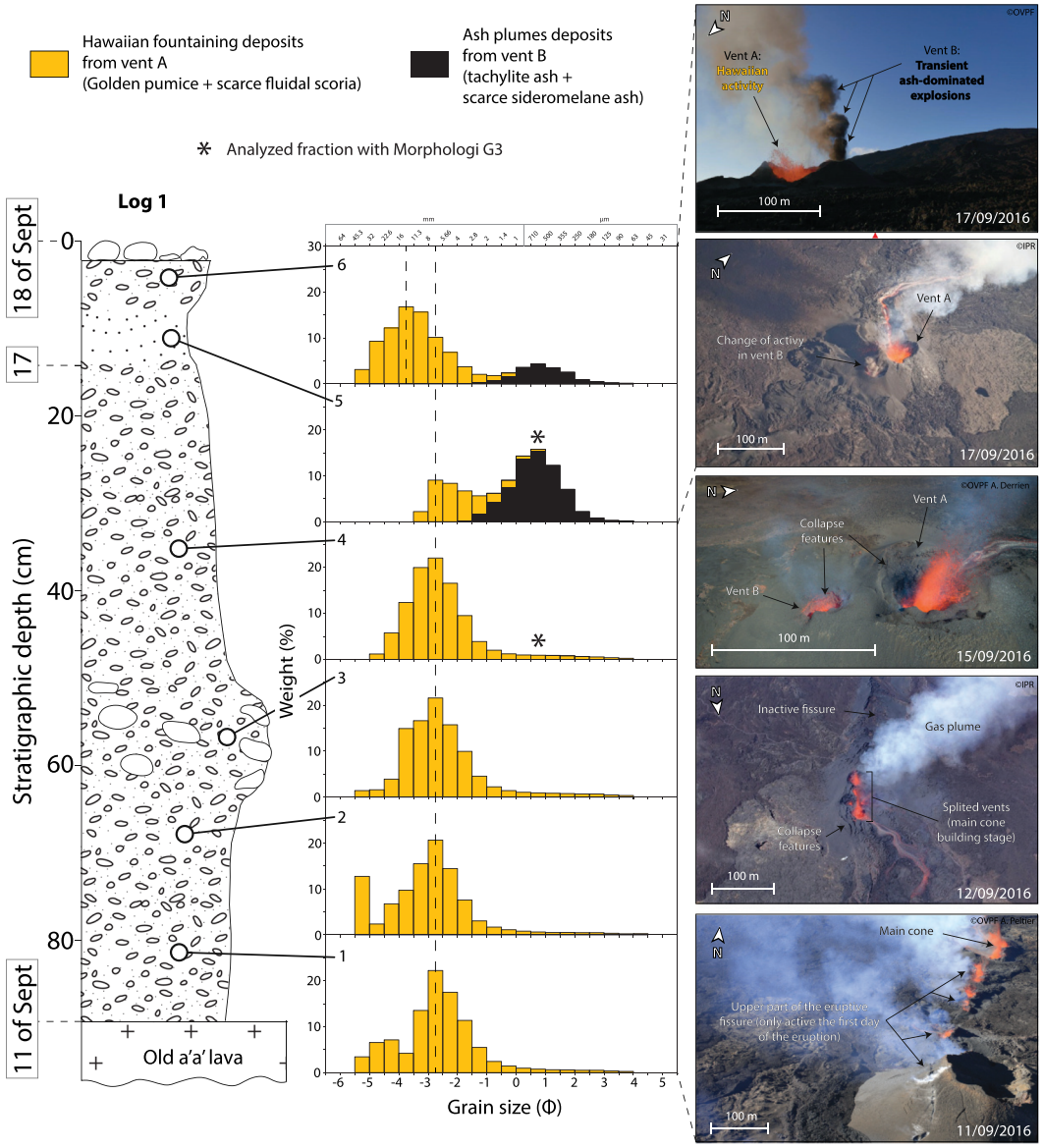

Figure 3. Stratigraphic log of the main section (Log 1), with corresponding grain size, componentry, and eruptive activity of the different sampled tephra beds.

all along the eruption. Golden pumice (Figure 5a) are characterized by highly vesicular, smooth, and yellowish glassy surface. Fluidal scoria (Figure 5a) are slightly denser and darker, still with a finely vesiculated glass. During the last day of the eruption, Vent B also produced some Hawaiian products coupled with (ii) sideromelane (dark color with more or less fluidal shape and a more or less rough surface, Figure 5a) and (iii) tachylite scoria (relatively dense with a dark, opaque rough surface aspect, Figure 5a). It is important to note that all the different juvenile components emitted by Vent B during the transient explosions are sometimes mingled together both at macroscopic and microscopic scale (Figures 5a and 5b), the golden, fluidal, or sideromelane components being always on the sample surfaces of the tachylite ones, as a coating and/or as an infiltration within small cracks. The amount of mingled clasts is relatively small compared to the nonmingled ones. The different ash components are genetically linked to the coarser material produced by the eruption (Figure 5). Hawaiian fountaining produced golden and fluidal ash coupled with some Pele's hairs and tears (Figure 5b). Pulsating activity from Vent B produced both sideromelane (brownish or gray color, Figure 5b) and tachylite ash (dark color, Figure 5b). Quantitative chemical analysis, petrographic observations, and textural measurements are described later in this paper,

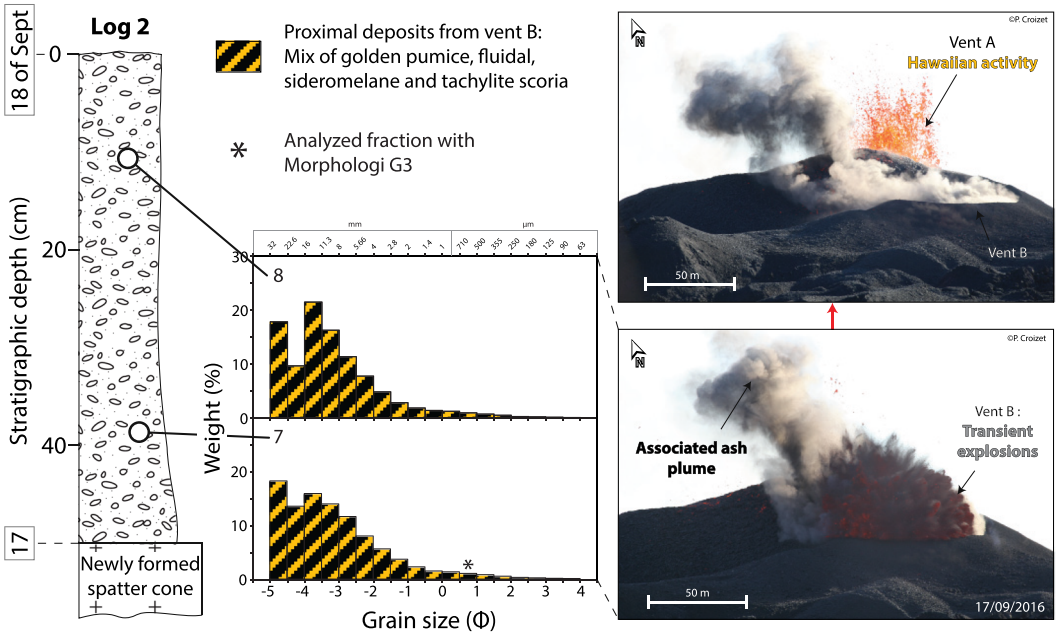

Figure 4. Stratigraphic log of the proximal Vent B section (Log 2), with corresponding grain size, componentry, and eruptive activity of the different sampled tephra beds.

but SEM images in Figure 5b provide an overview of the general texture of the different components. Microphenocrysts of olivine (ol) are observed in all the different pyroclast components and lavas, in different proportion depending on the time of the eruption (from 0 to 12 vol%), and these crystals are the biggest observed together with very scarce clinopyroxene (cpx) microphenocrysts (<1 vol%). Microphenocrysts of plagioclase (plg) are not observed. Golden and fluidal ash particles are highly vesicular with rounded vesicles and are poorly crystallized with very scarce and relatively small plg microlites and almost inexistent small cpx microlites. Sideromelane ash particles are less vesicular with both rounded and irregular-shaped vesicles and are more crystallized with small and slightly bigger microlites of plg and oscillatory zoned cpx microlites. This latter zoning has already been observed in other eruptions of PdF (DynVolc 2017) and may be attributed to variable crystal growth kinetic mechanisms under low-pressure conditions (Burkhard, 2005). Tachylite ash particles have relatively low vesicle content with irregular-shaped vesicles and are fully crystallized with both small and slightly bigger microlites of plg, in respect to the other components, and oscillatory zoned cpx as in the sideromelane component, associated with microlite of ol and micron-sized Fe-Ti oxides. These small oxides are also sometimes observed within the sideromelane component. The abundance of these Fe-Ti oxides is unusually high with respect to typical PdF products (DynVolc 2017).

4.2. Bulk Texture of the Bomb, Lapilli, and ash Size Fractions

Envelope density and bulk porosity (Figure 6a) as well as Helium vesicle connectivity (Figure 6b) measurements were performed on coarse fragments both from Vent A (all along the eruption) and Vent B (last day of the eruption, Table S2). Three fragments of lava, sampled near Vent A, were measured as well. Golden pumice and fluidal scoria are the most porous eruptive components, their density ranging between 0.3×10^3 and 1.5×10^3 kg m^{-3} (mode between 1.0×10^3 and 1.1×10^3 kg m^{-3}). No significant difference in porosity is observed between the golden pumice from Vents A and B. Sideromelane scoria densities range between 0.9×10^3 and 1.5×10^3 kg m^{-3} (mode at 1.0×10^3 kg m^{-3}), and tachylite scoria densities are slightly higher, between 1.2×10^3 and 1.8×10^3 kg m^{-3} (mode at 1.2×10^3 kg m^{-3}). The three lava samples have a density of 1.1, 1.2, and 1.4×10^3 kg.m^{-3}. Bulk porosity (Figure 6) was derived from the density using the measured Dense Rock Equivalent of 2.88×10^3 kg m^{-3}. Water pycnometry performed on ash size fractions (between 0.5 and 1 ϕ) leads to average porosities of 36, 14, and 7 vol% for the golden/fluidal, sideromelane, and tachylite ash, respectively.

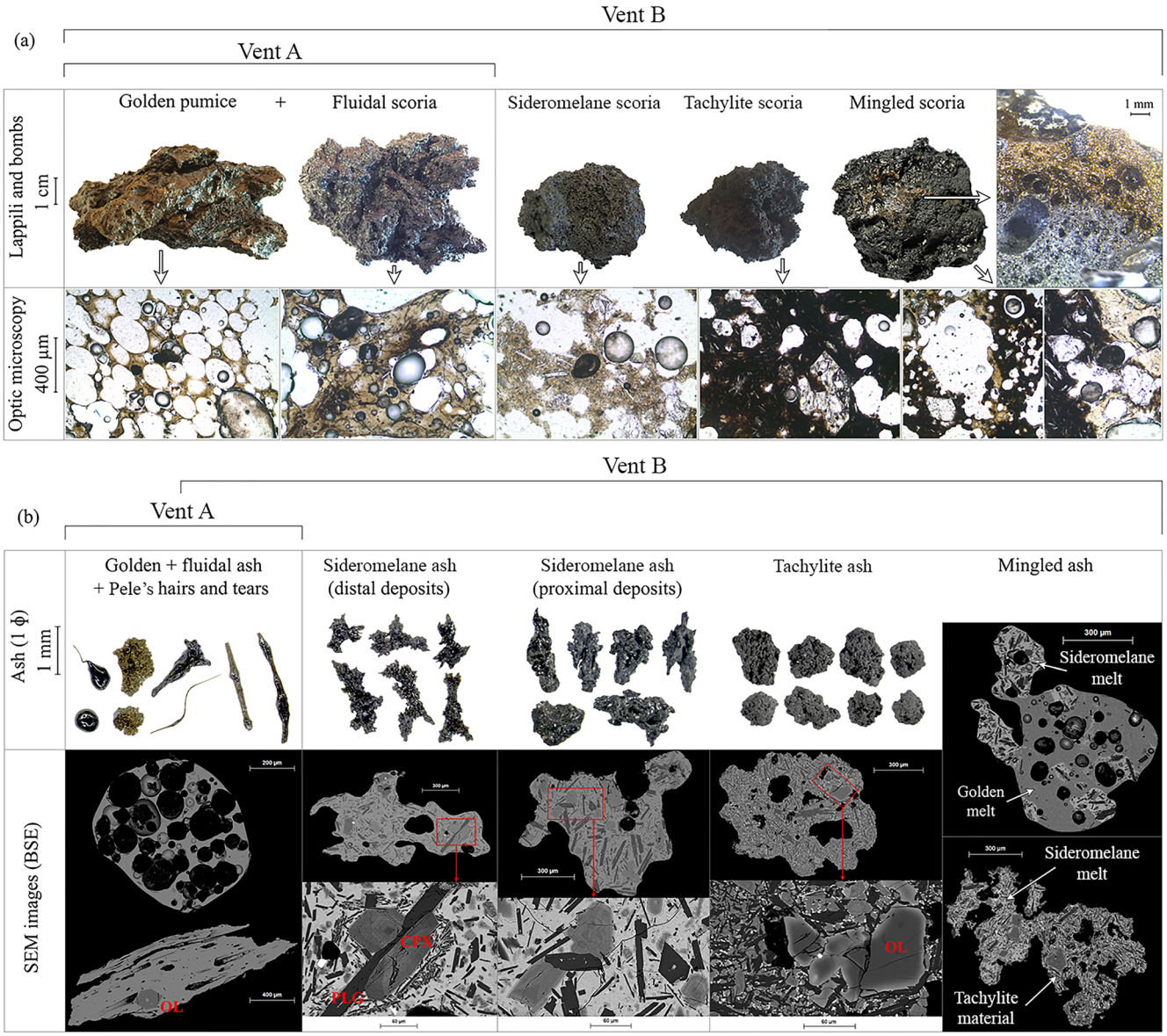

Figure 5. (a) Bomb-sized tephra componentry of the eruption, with corresponding thin section images with natural light. (b) Ash componentry, with corresponding BSE images.

Vesicle connectivity measurements are characterized by different trends for each identified component. The connectivity represents the percentage of vesicle volume interconnected. Golden pumice and fluidal scoria show the highest fraction of isolated vesicles, connectivity ranging between 57 and 100 vol% (81 vol % on average). On the other hand, sideromelane scoria vesicles are slightly more connected, connectivity ranging between 67 and 97 vol% (89 vol% on average), as well as tachylite scoria vesicles, which are almost all connected (between 96 and 100 vol%, 98 vol% on average). Three lava samples were measured, and they show 100 vol% of vesicle connectivity. Helium vesicle connectivity from the June 2014 and July 2015 eruptions are also shown (Gurioli et al., 2018; Thivet et al. submitted) and are relatively coherent with the September 2016 data. Vesicle connectivity data performed on the sideromelane scoria show intermediate values, reflecting the transition between low vesicle connectivity within the golden pumice (emitted during Hawaiian fountaining) and high vesicle connectivity within tachylite scoria for the September 2016 eruption and spiny scoria for the 2014–2015 pyroclasts (emitted during Strombolian-style or more explosive activity).

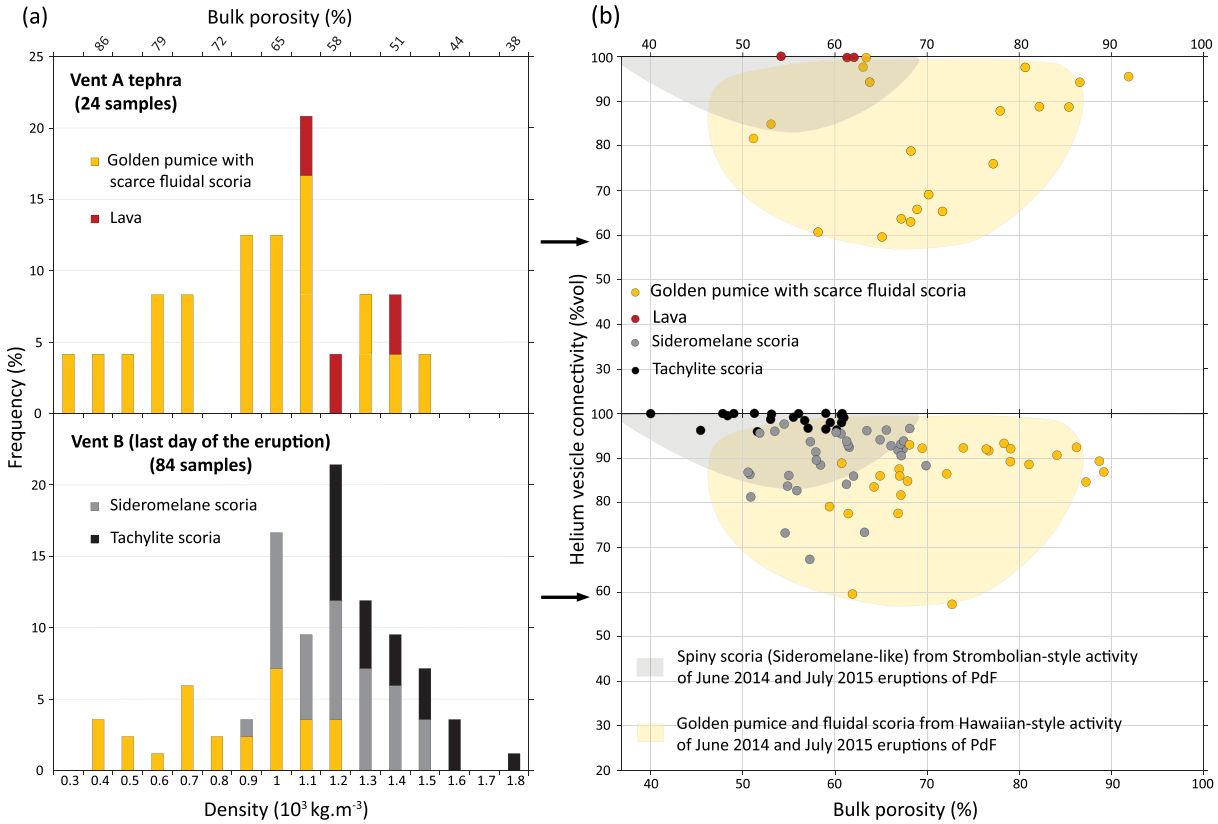

Figure 6. (a) Density and porosity measurements, displayed in histograms and normalized to the total number of samples for Vents A and B. (b) Helium vesicle connectivity measurements versus porosity.

Concerning the tephra permeability (Figure 7), most of the recent products analyzed (June 2014 and after) show a subhorizontal trend with porosity between 50 to 92 vol% and Darcian (viscous) permeability k_1 ranging between 10^{-11} and 10^{-9} m^2. Concerning the September 2016 eruption, the Hawaiian fountaining products are part of this trend while the sideromelane and tachylite scoria follow another trend with a decrease of k_1 (between 10^{-12} and 10^{-10} m^2) coupled with the decrease in porosity. Permeability measurements were also carried out on some products from the high explosive event of the 1860 violent strombolian eruption (Michon et al., 2013) and on some deposits of the energetic lava fountaining produced by the last Piton Chisny eruptive activity at PdF (Morandi et al., 2016; Principe et al., 2016). The measurements show

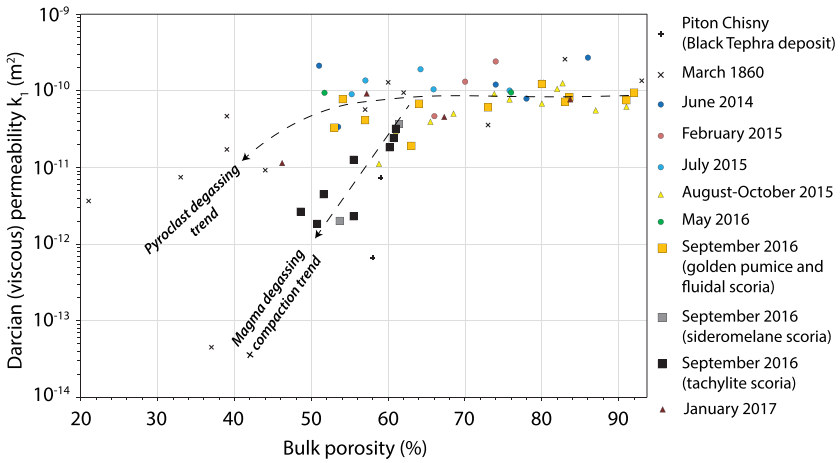

Figure 7. Darcian permeability (k_1) versus porosity of several samples from different eruptions of PdF.

a large range of permeability and porosity on these samples, especially for the 1860 products, which are very dense (down to 20 vol% of porosity) and relatively impermeable (down to 3×10^{-14} m^2).

4.3. Ash Morphometric Measurements

Morphometric measurements on each ash component (0.5–1 ϕ grainsize fraction) were carried out, and APASH data are represented on Figure 8. Solidity (morphological roughness, SLD) versus convexity (particle roughness, CVX) plot is represented and displays all the particle shapes for each component sample (Table S3). Each component has between 1,056 and 1,510 analyzed and filtered particles. This relatively high amount of particles (>1,000) is needed to be statistically representative of the emitted ash particles. These data show that each ash component has its own APASH signature. Golden/fluidal ash (yellow dots in Figure 8a) has a very large range of different ash shapes: The particles can be perfectly smooth and rounded particles (round droplets of vesicular melt, with SLD and CVX = 1) or can be relatively irregular, whose shape is reminiscent of vesicle walls (with SLD and CVX down to 0.55 and 0.60, respectively). A wide range of different particle shapes is observed between these two end-members and are basically formed by vesicular and glassy fragments. Pele's hairs and tears (red dots in Figure 8a), which are part of the same deposits of the golden/fluidal ash, have even more difference in shapes. These particles have approximately the same range in CVX (small-scale roughness, between 0.60 and 1) as the golden/fluidal ash, but they have a wider range in SLD (particle-scale roughness, between 0.25 and 1) reflecting particle elongation and deformation. The sideromelane APASH features (Figure 8b, SLD between 0.50 and 1, CVX between 0.60 and 1) look similar to the golden/fluidal ash components but without the hairs and tears component and have a slightly more spiny shape. Parameters measured in distal sideromelane ash samples (transported within ash plumes, Log 1; purple dots in Figure 8b) and proximal sideromelane ash samples (Log 2; green dots in Figure 8b) span a very similar range, with only a few differences that can be attributed to the condensate deposition observed on the proximal samples, whose effect is to slightly smooth the particle shape. Finally, tachylite APASH is significantly different from that of the other components (Figure 8c), with a narrow range of both SLD (0.75 to little bit less than 1) and CVX (0.85 and little bit less than 1 as well). These values reflect a relatively high degree of roundness but with a high amount of small scale irregularities. Rounded particles with SLD and CVX at 1 (like found in the golden/fluidal and sideromelane components) are not observed any more within the tachylite ash. Statistical analysis represented in boxplots (Figure 8d) highlights that both SLD and CVX increase from the golden/fluidal ash + hairs/tears, to sideromelane ash, to tachylite ash, in terms of median value (red lines) as well as 25th and 75th percentile (blue boxes, which englobe the half of each data set). Also note that the boxplot whiskers (which represent approximately the 2.7 σ boundaries of each data set), as well as the outliers (data outside 2.7 σ represented by the red crosses), are progressively closer to the median from the golden/fluidal ash and hairs/tears particles, to sideromelane ash, to tachylite ash. AR of each component is also represented and shows that particles are progressively more elongated from the tachylite, to the sideromelane, until the golden/fluidal and Pele's hairs and tears components.

4.4. Chemical Analysis of the Bomb, Lapilli, and Ash Size Fractions

4.4.1. Bulk Rock and Glass Compositions

Major and minor element analyses of bulk rocks and glasses (Table S4) were performed in order to constrain potential pre- and syn-eruptive variations of the magmatic composition. Bulk rock analyses were performed on all the different pyroclastic components, including a lava fragment.

The comparison between the August–October 2015 bulk rock compositions with the May and September 2016 ones (Figure 9) reveals several notable facts. (i) It shows that the magma erupted in August–October 2015 was first relatively differentiated and olivine-free (around 0.8 in CaO/Al_2O_3, 6.5 wt% in MgO and 0.7 wt% in K_2O) but then become progressively more mafic and olivine-rich toward the end of the eruption (up to 0.9 in CaO/Al_2O_3, 11.0 wt% in MgO, and down to 0.6 K_2O wt%). (ii) Then, the May 2016 eruption emitted an olivine-rich magma (0.8 in CaO/Al_2O_3 and 9.1 wt% in MgO) and exhibit a wide range in K_2O (from 0.6 to 1.1 wt%). (iii) Focusing on the September 2016 eruption, the magma emitted was first relatively differentiated (0.8 in CaO/Al_2O_3) and K_2O-poor (0.8 wt% in K_2O, without ol phenocrysts 6.5 wt% in MgO).

Similarly to some recent eruptions at PdF, the magma of the September 2016 eruption is progressively olivine-bearing (cf. the trends of increasing amount of ol in Figure 9). The high variability in MgO is attributed to the variable abundance of the ol microphenocrysts that increase toward the end of the eruption: considering (i) an average MgO content in the golden pumice liquid of 6.5 wt%, (ii) an average MgO content in

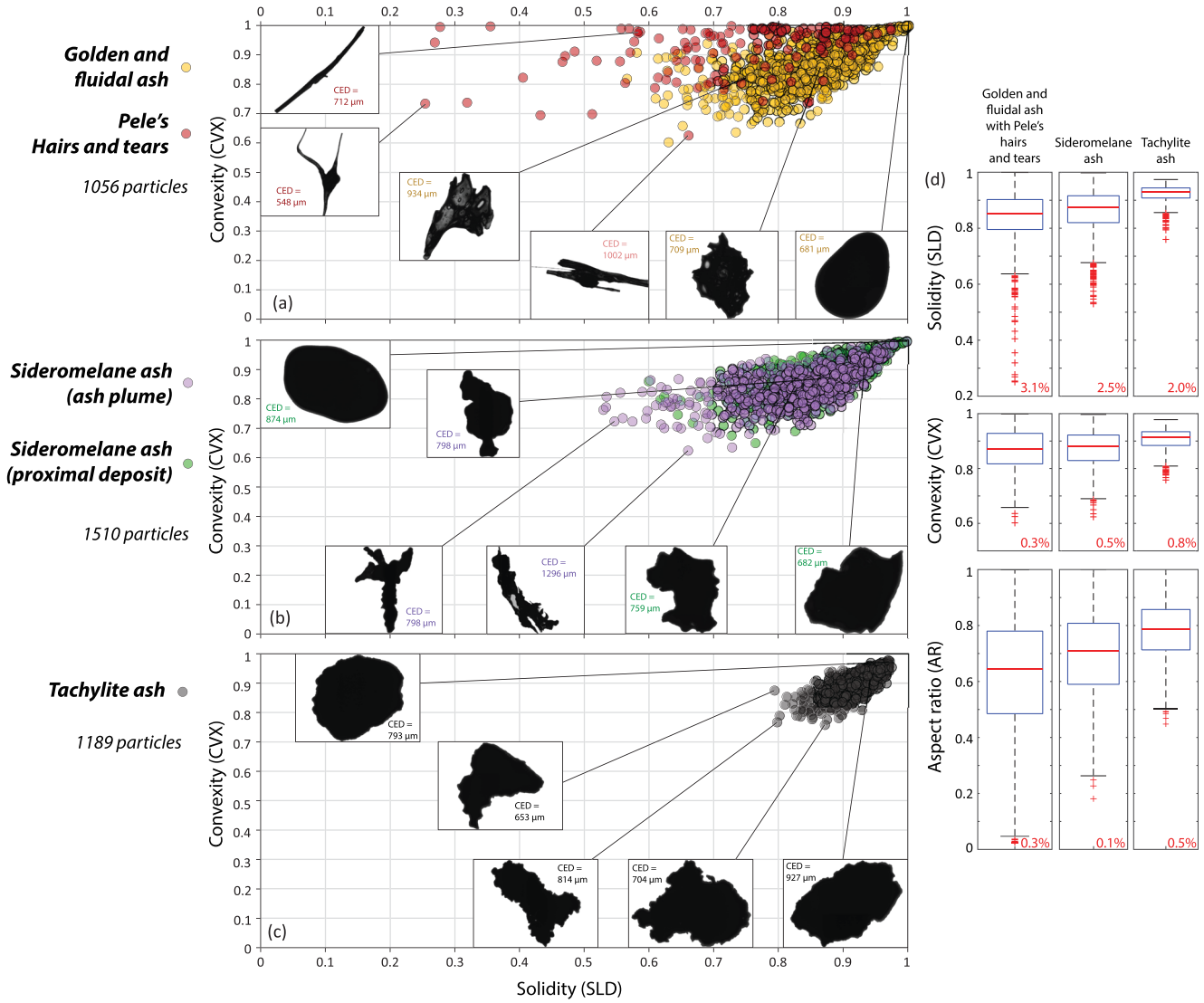

Figure 8. Morphometric (APASH, solidity vs. convexity) data set of each ash component at 0.5–1 ϕ grain size fraction. (a) Golden/fluidal ash with Pele's hairs and tears, (b) sideromelane ash, and (c) tachylite ash. (d) Statistical analysis of each component data set on boxplots for solidity, convexity, and aspect ratio of the particles. Middle red lines represent the median, blue boxes represent all the particles between the 25th and 75th percentiles (englobes 50% of the data set), boxplot whicker boundaries represent 2.7 σ of the data, and red crosses represent each ash particles outside this boundary (outliers).

the ol phenocryst of 43.3 wt%, and (iii) a MgO content in the bulk rock compositions ranging between 6.5 and 11.1 wt% (cf. sections here after for these values, Table S4), we were able to estimate by mass balance the ol phenocrysts content (X_{ol}) between 0 vol% (11 September sample without ol) and 12 vol% (17 September, most ol-rich sample). Moreover, since 16 September, we observed the occurrence of K_2O-richer magmas (mostly fresh golden pumice and lava) whose compositions range between 0.8 and 1.1 wt% in K_2O (compositions in between the K_2O-poor magmas of August–October 2015 and the K_2O-rich May 2016 end-member). It is important to note that the two tachylite scoria fragments analyzed have the same composition of the initial K_2O-poor golden pumice. On the other hand, the analyzed sideromelane and tachylite ash particles have K_2O-rich compositions.

Because the eruption produced a large amount of ash compared to the other recent eruptive fissures at PdF (DynVolc 2017), we mostly focused on the ash particles to perform the glass composition measurements, petrology analysis, and the microtexture characterization. Moreover, we suggest that the ash can conserve the more pristine signature of the fragmentation processes because of the relatively fast natural quenching in air (D'Oriano et al., 2014; Di Muro et al., 2015; Potuzak et al., 2008; Porritt et al., 2012;

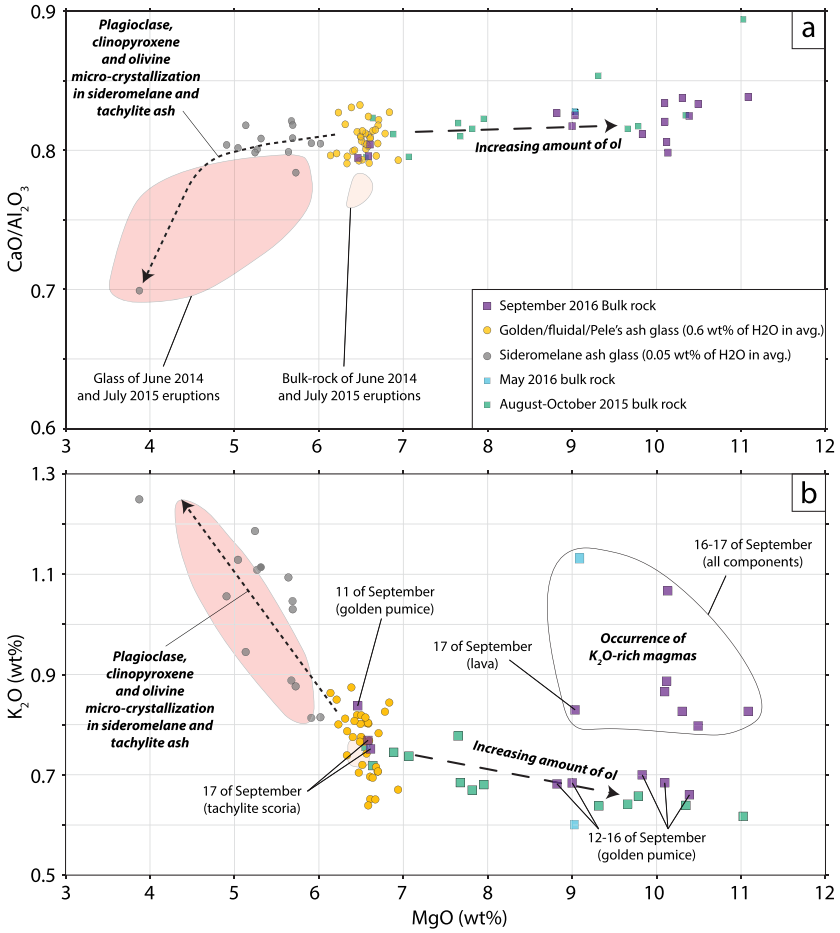

Figure 9. Bulk rock and in situ glass compositions (MgO vs. CaO/Al_2O_3) of the eruptive products.

Pompilio et al., 2017; Xu & Zhang, 2002) compared to the large lapilli and the inner parts of the bomb-sized tephra. The golden/fluidal glass compositions (Figure 9) range between 6.14 and 6.94 wt% in MgO, between 0.79 and 0.83 in CaO/Al_2O_3, and between 0.64 and 0.87 wt% in K_2O. Considering the analytical uncertainties (Table S4), they thus encompass the ol-free bulk-rock compositions, and this is consistent with a crystal-poor matrix. Sideromelane glass is characterized by a wider range of composition reflecting different degrees of crystallization of relatively Na-rich plg, cpx, and relatively Fe-rich ol (between 3.88 and 6.47 wt% MgO, between 0.70 and 0.83 in CaO/Al_2O_3, and between 0.70 and 1.25 wt % in K_2O), with a relatively similar compositional trend as observed for the 2014–2015 matrix. No glass has been observed in the tachylite component.

4.4.2. Mineral Assemblage and Compositions in the Ash Particles

The different mineral phases present in the eruptive products are plg, cpx, Fe-Ti oxides, and ol in order of abundance, without considering the increase of ol microphenocrysts toward the end of the eruption. On the basis of the crystal size, shape, and compositions, we identify four distinct crystal populations within the September 2016 eruptive products that are listed in order of appearance within the erupted magma.

1. First, the compositions of the euhedral ol microphenocrysts range between $Fo_{78\text{-}84}$. Mg-Fe distribution coefficients (K_D) between these ol and bulk rock composition are on average 0.24, which show that most of these ol are too rich in Mg considering our bulk rock composition (equilibrium reach at $K_D = 0.30 \pm 0.03$, Putirka, 2008). In order to calculate the FeO content of the cumulative ol-free bulk rock composition (6.46 wt% in MgO and 10.16 wt% in FeO), we used an average Fe^{3+}/Fe_{total} ratio of 0.18 for La Réunion island basaltic melts (Pichavant et al., 2016). We thus conclude that most of these ol microphenocrysts originate from cumulative processes (22 analyzed crystals with Fo > 80), and only a few crystals are in equilibrium with the pre-eruptive/bulk rock melt (six analyzed crystals with

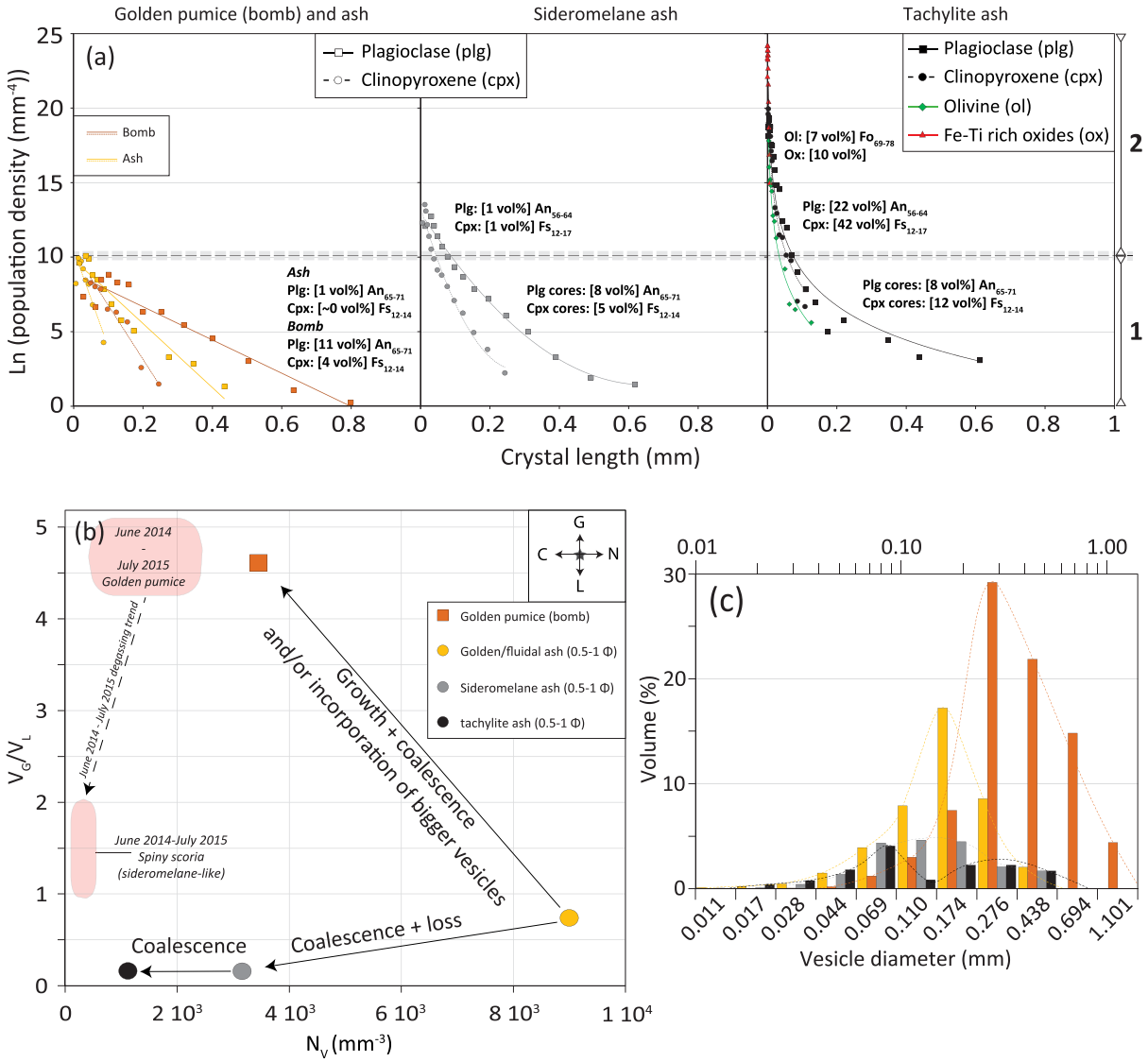

Figure 10. (a) CSDs of the different components with associated crystal contents and compositions. Field 1: golden microlites + inherited big microlites (>0.05 mm) of the sideromelane and tachylite components. Field 2: small microlites (<0.05 mm) of the sideromelane and tachylite components + ol and ox microlites of the tachylite component. (b) N_V versus V_G/V_L of the different components. G = bubble growth; N = bubble nucleation; L = gas loss; C = bubble coalescence. (c) VSDs of the different components.

Fo_{78-80}). The ol microphenocrysts content varies from 0 (beginning of the eruption) to 12 vol% (end of the eruption) within each eruptive component, and these crystals are the largest observed in the September 2016 products (up to 600 μm in length and 400 μm in width). Scarce ol-free microphenocrysts are observed in the ash produced by Vent B the last day of the eruption in grain size fraction lower than 2 ϕ.

2. The second crystal population is represented by the euhedral microphenocrysts in equilibrium with the bulk rock composition, namely, the scarce ol microphenocrysts (Fo_{78-80}) described previously associated with very scarce cpx microphenocrysts (only one agglomerate of three cpx crystals observed within the golden/fluidal component, with around 500 μm in length and 300 μm in width for each crystal). These crystals represent <1 vol% in all the eruptive components. The cpx crystals in equilibrium (K_D of 0.25 on average, equilibrium reach at 0.28 ± 0.08, Putirka, 2008) have a composition range of Wo_{44-46} En_{45-47} Fs_{9-10}.
3. The third crystal population (field 1 in Figure 10a) is represented by the microlites (plg and cpx) of the golden component (>0.05 and >0.02 mm for plg and cpx, respectively) as well as the cores of the

slightly bigger microlites of the sideromelane and tachylite components (plg and cpx). Their compositions range between $An_{65-71}Ab_{28-34}Or_1$ for the plg and $Wo_{35-46}En_{41-52}Fs_{12-14}$ for the cpx. Their occurrence depends on the components (Figures 5 and 10a).

4. The fourth and last crystal population to form (field 2 in Figure 10a) is represented by the small microlites (<0.05 and <0.02 mm for plg and cpx, respectively) of plg, cpx, oxides, and ol (with some rims of bigger crystals) that form within the sideromelane and tachylite components (Figure 5). Their compositions ($An_{56-64}Ab_{34-41}Or_{1-3}$ for plg, $Wo_{37-44}En_{39-49}Fs_{12-17}$ for cpx, and $Fo_{69-78}Fa_{21-30}$ for ol) are the richest in Na for the plg and the richest in Fe for the cpx and ol. The micron-sized oxides observed in the tachylite component are rich in Fe and Ti. As well as the latter microlite population, their occurrence depends on the components (Figures 5 and 10a).

Both population of microlites (small and large plg and cpx of all the components) are in equilibrium with their surrounding glass: $K_D = 0.25$ on average for plg, using the plg-melt equilibrium constant of Putirka (2008) calibrated for melts whose temperature exceeds 1,050 °C (An-Ab $K_D = 0.27 \pm 0.11$ at equilibrium), $K_D = 0.30$ on average for cpx (equilibrium reached at $K_D = 0.28 \pm 0.08$). K_D for ol microlites cannot be calculated because these crystals only occurred in the tachylite component that lacks interstitial glass, which suggests that ol microlites, with the micro-ox, are the latest phases to crystallize.

4.4.3. Magma Temperature and H_2O Content Estimations

We then used the two MgO-thermometers of (cf. Figure S2) calibrated (experimental data) for (i) undegassed and pre-eruptive conditions (using bulk rock and golden pumice glass compositions, T (°C) = 27.5 MgO^{liq} + 943.7) and for (ii) degassed and syn-eruptive eruptive conditions (using sideromelane glass compositions, T (°C) = 17.7 MgO^{liq} + 1041.7). Ol-free bulk rock composition (6.46 wt% of MgO), which represents the initial magma composition, leads to a calculated magma temperature of 1,121 °C. In parallel, the golden pumice component (which do not have significant microlite and thus do not exert microcrystallization yet) whose glass composition is similar to that of the bulk rock (6.55 wt% of MgO on average) leads to melt temperatures between 1,112 and 1,134 °C (1,124 °C on average). Using the Lange et al. (2009) hygrometer based on the plg-melt equilibrium (An-Ab $K_D = 0.27 \pm 0.11$ at equilibrium; Putirka, 2008), we can estimate the dissolved H_2O content of the magma. We used both plg microlite compositions and glass compositions that are in equilibrium, in order to estimate the dissolved H_2O content within the eruptive products, which leads to calculated H_2O content between 0.3 and 0.7 wt% (0.6 wt% on average) for the golden pumice. On the other hand, the estimated sideromelane melt temperatures range between 1,110 and 1,148 °C and dissolved H_2O contents range between 0.0 and 0.2 wt% (0.05 wt% on average).

4.5. Crystal Contents and Size Distributions

CSDs were measured on the ash particles in order to study crystals that did not form due to postfragmentation cooling, but which likely nucleated and grew by degassing during the magma ascent toward the surface and cooling at very shallow levels. Microphenocrysts could not be taken in account in these textural measurements because they were too scarce both in the ash particles and as free crystals. We only focus on the two microlite populations previously described that are representative of the syn-eruptive crystallization of the magma.

The golden/fluidal ash is almost crystal free (Figure 10a) with only 1 vol% (all the crystal contents are corrected for porosity and microphenocryst content) of small microlites of plg (<0.5 mm in length) and very scarce small microlite of cpx (<0.1 mm in length). In parallel, the crystal content of the golden pumice (bomb-sized) is higher (15 vol%) with 11 vol% of small microlites of plg (<0.8 mm in length) and 4 vol% of small microlites of cpx (<0.3 mm in length), which confirmed that coarse clasts can contain postfragmentation crystallization. Golden/fluidal ash CSDs of plg and cpx show linear trends (CSD slopes of −21.49 and −65.14 mm^{-1}, respectively), with relatively low nucleation densities N^0 ($e^{9.84}$ and $e^{10.47}$ mm^{-4} for plg and cpx, respectively; these values are the population densities at crystal length = 0) and low number density of crystals N_C (1.1×10^3 and 4.0×10^2 mm^{-3} for plg and cpx, respectively, Table S5). Golden pumice CSDs show similar characteristics as the golden/fluidal ash, except that their linear CSD slopes are slightly gentler, reflecting longer crystallization time (Figure 10a). For the next components, we only focused on the ash fraction.

The crystal content of the sideromelane ash component (Figure 10a) is higher than in the golden ash (17 vol %) with 9 vol% of plg and 6 vol% of cpx, with also higher nucleation densities N^0 (around ln(13) mm^{-4}) and higher crystal number density N_C (1.2×10^4 and 2.4×10^3 mm^{-3} for plg and cpx, respectively). Crystal lengths are slightly higher than the ones in the golden ash (<0.6 and <0.4 mm for plg and cpx, respectively). The bigger microlites are also wider (Figure 5b), but this parameter does not appear in the CSD measurements as CSD plots only show the crystal lengths. These wider crystals are nevertheless distinguishable in the CSD as they are characterized by the same range of population densities as the golden/fluidal ash microlites (< ln(10) mm^{-4}). On the other hand, small microlites (<0.05 and <0.02 mm in length for plg and cpx, respectively) show more sodic An_{56-64} and ferric Fs_{12-17} compositions, associated with higher population densities than the golden microlites and the sideromelane big microlites (>ln(10) mm^{-4}). It is also important to note that the CSD slopes of the sideromelane component are not linear as the golden ones but slightly curved with relatively steep slopes for small microlites and relatively gentle slopes for the largest crystals compare to the golden/fluidal ash linear CSD (Figure 10a).

The tachylite ash component is 100 vol% crystallized with 54 vol% of cpx, 30 vol% of plg, 10 vol% of Fe-Ti micron-sized oxides, and 7 vol% of ol on average (optical microscopy observations confirmed that bomb-sized tachylite scoria are also 100 vol% crystallized, Figure 5a). Crystal number densities are the highest of the three different eruptive components (1.6×10^6, 1.5×10^6, 9.0×10^4, and 5.4×10^7 mm^{-3} for plg, cpx, ol, and oxides, respectively). Crystal length are approximately the same as the previous components (<0.5 and <0.2 mm for plg and cpx, respectively), but some plg and cpx crystals are wider than the ones of the golden component. We observed the same plg and cpx crystals populations as in the sideromelane CSDs (small and larger microlites with the same composition evolution). However, the occurrence of micron-sized oxides (<0.01 mm in diameter) and Fo_{69-78} ol (<0.2 mm in length) contrasts with the absence of these late crystallized phases within the golden and sideromelane components. Moreover, the ol microphenocrysts are often normally zoned in the tachylite component (Fo_{79-84} on the cores and down to Fo_{72} on the rims); this normal zoning is only observed within the tachylite component. As in the sideromelane component, the CSD slopes of the tachylite component are not linear but slightly curved with relatively steep slopes for small microlites and relatively gentle slopes for the largest crystals compare to the golden/fluidal ash linear CSD (Figure 10a).

4.6. Vesicle Content and Size Distributions

The golden pumice/fluidal scoria component is relatively porous (Figure 6a) with an average of 72 vol% of vesicles (from 48 to 89 vol%). Water pycnometry measurements on the golden/fluidal/Pele ash (0.5–1 ϕ) lead to a much lower average vesicularity of 36 vol% (from 35 to 38 vol%, Table S2). Vesicles are rounded and elongated in the Pele's hairs and tears, but they do not show evidence of coalescence. For different particle size of a same component, a large difference is observed in porosity. We thus performed microtexture analysis (Table S5) on one golden pumice thin section from a 10 cm large bomb emitted by Vent A, in order to quantify the differences between coarse and fine material (as in the previous section for the crystal analysis). In spite of the difference in vesicularity, the N_v values of the ash and the golden bomb are both up to 10^3 mm^{-3}. The VSD (Figure 10c) of the golden ash show only one population of vesicles, from a few microns to 0.4 mm in diameter, with a mode around 0.2 mm in diameter (V_G/V_L of 0.7 and N_V of 9.0×10^3 mm^{-3}). Concerning the golden pumice textural analysis, we also found one population of vesicles, but it is skewed toward bigger size, from around 40 μm to 1.1 mm in diameter, with a mode around 0.3 mm in diameter (V_G/V_L of 4.6 and N_V of 3.4×10^3 mm^{-3}). Note that the porosity estimated for the ash fraction with the microtexture counting the vesicles (42 vol%) is quite coherent with the water pycnometry measurement (36 vol%).

Sideromelane scoria is less porous than the latter component (Figure 6a) with an average value of 61 vol% (from 47 to 68 vol%). Water pycnometry measurements on the sideromelane ash (0.5–1 ϕ) lead to an average vesicularity of only 14 vol% (from 11 to 16 vol%). Sideromelane ash has a low V_G/V_L ratio of 0.2 and a N_V of 3.2×10^3 mm^{-3} (Figure 10b), reflecting bubble coalescence and loss from the golden ash. Its VSD show a unimodal population (Figure 10c) with relatively low vesicle volume (porosity of 13 vol% coherent with the water pycnometry measurements). Vesicle sizes range from around 20 μm to 0.4 mm, with a mode around 0.1 mm. Vesicles can be ever rounded or irregular-shaped.

Tachylite component represent the more degassed and crystallized component with an average value of porosity of 54 vol% (from 38 to 58 vol%) concerning the lapilli- and bomb-sized pyroclasts (Figure 6a) and 7 vol% (from 7 to 8 vol%) for the ash fraction. This ash component has a very low V_G/V_L ratio of 0.2 and a N_V of 1.1×10^3 mm^{-3} (Figure 10b), reflecting further bubble coalescence with respect to the sideromelane ash. The VSD shows very low vesicle volume (porosity of 10 vol% coherent with the water pycnometry measurements) from around 20 μm to 0.4 mm in vesicle diameter (Figure 10c). Two potential modes are observed, the first one at 70 μm, which is slightly lower than the modes of the golden/fluidal and sideromelane ash (which might reflect gas loss) and the second one around 0.3 mm, which is higher than the other ash components and is represented by irregular-shaped vesicles, which might reflects coalescence.

Comparing the V_G/V_L and N_V values of the September 2016 eruption with those measured for the June 2014 and July 2015 eruptions (Gurioli et al., 2018; Thivet et al. submitted), slightly different trends appear. This comparison shows that the vesicles are more abundant in the September 2016 golden pumice than in the June 2014 and July 2015 ones, in term of N_V, which highlight a slightly higher nucleation rate for the September 2016 golden pumice.

5. Discussion

5.1. Eruptive Trigger

One of the main challenges of typical dyke eruptions at PdF, as the September 2016 one, is to characterize their precursors to understand their triggers mechanisms and anticipate their starting and evolution. This eruption was preceded by several midterms precursors as the slight increase in the ground gas emission, the change of gas compositions within the summit fumarole, and the increase in the seismicity (Peltier et al., 2018). However, and similarly to the short-lasting eruptions of June 2014 and May 2016, slight ground inflation was detected just shortly before the eruption. For the June 2014 eruption, this relatively late ground inflation was interpreted by Gurioli et al. (2018) as the pre-eruptive second boiling process that trigger the eruption a few days later, but no evidence of a new input of magma was found. Instead, clear evidences of rejuvenation were found during the long lasting and voluminous eruption of August–October 2015 that lasted almost 2 months and was characterized by different ground inflation trends (Coppola et al., 2017; Peltier et al., 2018). The first question is where the 2016 eruption is placed between these two end-member behaviors?

The September 2016 lava flux evolution is quite similar to that measured during typical eruptions at PdF (Hibert et al., 2015 for the January 2010 eruption; Coppola et al., 2017, for the 2014–2015 eruptions) with nevertheless a few important and notable characteristics. The absolute values of these measured lava flux are higher than those observed during the small eruptions of the 2014–2015 period documented by Coppola et al. (2017), namely, the June 2014 (maximum lava flux around 7 m^3 s^{-1}), February 2015 (maximum lava flux around 2 m^3 s^{-1}), May 2015 (maximum lava flux around 35 m^3 s^{-1}), and July 2015 (maximum lava flux around 22 m^3 s^{-1}) eruptions. However, the September 2016 lava flux values are comparable to that measured during the August–October 2015 eruption. Similarly to this later eruption, we also observed a late increase in the lava flux for the September 2016 eruption (Coppola et al., 2017). However, for the August–October 2015 eruption, this late increase in lava flux was correlated with a deep recharge of the magmatic system and the emission of relatively pristine magmas (high MgO and CaO/Al_2O_3 content) without ash emission, while during the September 2016 eruption, the late increase in lava flux was correlated to the change in activity style with ash and bomb emission but without the emission of pristine magmas. Indeed, the bulk rock chemical evolution since 2014 at PdF suggests that the rejuvenation of the shallow plumbing system began to be evidenced with the July and August–October 2015 eruptions (Coppola et al., 2017). However, the September 2016 erupted magma is not as pristine as the August–October ones but was quite differentiated (Figure 9a). The lack of deep input is also supported by the relatively low SO_2 emissions. Thanks to the conversion lava flux-SO_2 flux established in a previous study (equation 5 in Hibert et al., 2015), we can estimate the SO_2 flux considering a given lava flux and the porosity of the magma at the fragmentation level. Using the initial lava flux peak (between 30 and 50 m^3 s^{-1}, Figure 2d) and the golden pumice porosity (between 60 and 70 vol%, Figure 6 a), the estimated SO_2 flux is very coherent with the measured one of 2,500 tons day^{-1} (Figure 2e) only if

we considered a pre-eruptive degassed magma condition (that contrast with a primitive gas-rich magma). A similar reasoning is also applicable to the entire eruption, thus involving a relatively degassed magma, even during the increase of the lava flux at the end of the eruption (Figures 2d and 2e). Moreover, no textural and chemical features evidence any pre-eruptive magmatic inputs. In summary, we state that the magma emitted during the September 2016 eruption is not compatible with the contribution of a relatively deep and gas-rich magma and is rather coherent with a partial degassed shallow magma. The ubiquity of golden pumice in the eruptive deposits, similarly to the beginning of the June 2014 eruption, suggest that this differentiated magma experienced significant pre-eruptive bubble nucleation. We therefore suggest that the first phase of the eruption associated with the emission of chemically differentiated golden pumice and typical decreasing lava flux trend until 13 September (Figure 2d) was triggered by similar pre-eruptive second boiling mechanism as the June 2014 eruption (Gurioli et al., 2018).

5.2. Eruptive-Style Evolution

Since 16 September and toward the end of the eruption, K_2O-rich magma appeared (Figures 2e and 9b). This reflects the emission of a different magma, with respect to the first days of the activity, which have intermediate compositions ranging between the initial differentiated magma (11 September) and the May 2016 K_2O-rich magma (Figure 9). The occurrence of this K_2O-rich magma during the September 2016 eruption could be eventually linked with the tremor and lava flux fluctuations since the 16 (Figures 2a, 2b, and 2d) and the progressive increase of these signal intensities during the 17 of September. The slight decrease of the volcanic tremor (Figures 2a and 2b) can be linked to the significant decrease of the activity in Vent B, while Vent A remained relatively active. We thus suggest that both subsurface eruptive conduit and scoria cone edifice geometry evolutions induced changes in the observed activity at the surface (Pioli et al., 2017). During the 17th, the activity increased in terms of volcanic tremor, lava flux (between 15 and 40 $m^3\ s^{-1}$; Figure 2d) and both bomb and ash emissions from Vent B (Figure 4) whereas Vent A remained active with typical Hawaiian-style activity (Figure 3). Although this increase of intensity (associated with the arrival of the K_2O-rich magma) probably helped the resumption of the activity, it cannot be the only explanation of the unusual high degree of fragmentation produced at Vent B, as we already observed the same relative intensity at the beginning of the eruption, but without significant pulsating ash emission. The second and main question of this study is what are the mechanisms linked with this eruptive-style change?

5.2.1. Golden and Fluidal Scoria/Ash Ubiquity Representative of a Not Completely Degassed Magma Associated With Open-Vent Hawaiian Fountaining Activity

The presence of Hawaiian fountaining all along the eruption (Vent A), mainly produced golden pumice with scarce fluidal scoria. We suggest that the golden pumice represent the fragmented material that stays the longest within the central part of the lava fountain, as already documented in strong Hawaiian-style activity (e.g., Parcheta et al., 2013; Stovall et al., 2011, 2012) and in the relatively mild Hawaiian-style activity of PdF (Gurioli et al., 2018). Theoretically, the difference in porosity can be explained mostly by postfragmentation bubble expansion (V_G/V_L of 4.6 and N_V of $3.4 \times 10^3\ mm^{-3}$) that occur in coarse clasts (Figure 10b), compared to ash particles (V_G/V_L of 0.7 and N_V of $9.0 \times 10^3\ mm^{-3}$) that, of course, do not have bubbles bigger than their own particle size but also do not show evidence of coalescence or growth. However, bubble growth of the golden pumice within the short-lived lava fountaining at PdF is not as significant as in the Hawaiian reticulites (Mangan & Cashman, 1996) as we observed relatively high amount of isolated vesicles in the golden pumice and fluidal scoria (up to 40 vol%; Figure 6b) and relatively high Nv (see also Figure 11 in Gurioli et al., 2018). Thus, we suggest that the higher vesicularity of the golden pumice is more representative of the magmatic conditions at fragmentation, whereas the lower vesicularity of the ash is explained by the relatively small size of the ash facilitating the gas to escape. However, the higher Nv of the ash confirmed the capability of this fine material to preserve the pristine vesicle nucleation number (Figure 10b).

Crystal contents and size distributions (Figure 10a) also show that microlites in the large golden pumice are slightly bigger (maximum length of 0.8 mm) than the ones in the ash fraction (maximum length of 0.5 mm). This evidence suggests that the former grew during a longer residence time within the lava fountains (relative slight CSD slope) than the golden/fluidal ash microlites (steeper CSD slope). Moreover, very few and relatively small rounded vesicles are observed among all the highly deformed vesicles within the Pele's hairs and tears, which suggest relatively short time between the bubble deformation (postfragmentation) and

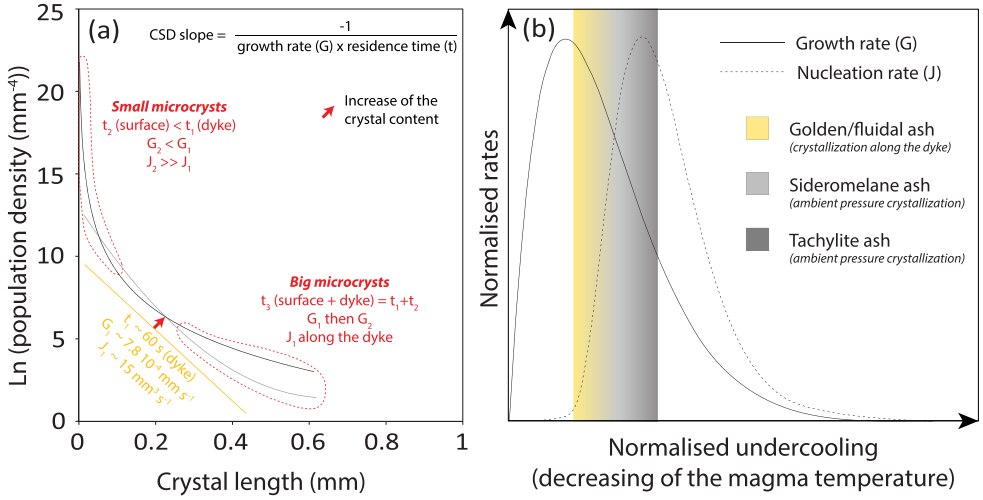

Figure 11. (a) Interpretation of the plg CSD evolution of the three different eruptive components (the yellow, gray, and black lines are, respectively, representative of the golden pumice, sideromelane, and tachylite plg microlites). (b) Evolution of the crystal growth (G) and nucleation (J) rates as a function of the degree of undercooling (modified from Higgins, 2000).

quenching (Cannata et al., 2019). D'Oriano et al. (2014) also suggest that the microlites cannot grow significantly after the ash emission considering reasonable quenching rates of 20 °C s^{-1} (Xu & Zhang, 2002) and maximum crystal growth rates of 2×10^{-5} mm s^{-1} for plg and 6×10^{-6} mm s^{-1} for cpx (cf. following paragraphs). All these latter points suggest that the golden ash fraction experienced almost immediate and efficient quenching after the fragmentation, compared to bomb-sized pyroclasts.

In accordance with Di Muro et al. (2015) and Gurioli et al. (2018), we suggest that the microphenocrysts of ol and cpx observed in the eruptive products are formed before the magma degassing by cooling-driven crystallization in the magma reservoir. On the other hand, we support that the microlites observed in the eruptive products (plg, cpx, micro-ol, and oxides) are first formed by degassing-driven crystallization during the eruption (golden component) and then continued to form and grow during the progressive cooling and degassing of the sideromelane and tachylite components at very shallow levels (cf. following section). Focusing on the ash fraction, the golden/fluidal ash is characterized by an almost microlite-free (1 vol%; Figure 10a) matrix. Microlite compositions show intermediate compositions ($An_{65\text{-}71}$ for plg and $Fs_{12\text{-}14}$ for cpx), coherent with the degassing-driven crystallization composition range recorded during previous eruptions. The average H_2O content in this melt is 0.6 wt% with an average temperature of 1,124 °C, showing that this melt is not completely degassed (disequilibrium exsolution during the magmatic ascent). Moreover, unimodal VSD (Figure 10b) and linear CSD (Figure 10c) suggest that this magma experienced one event of bubble and crystal nucleation and growth within the eruptive dyke.

According to Di Muro et al. (2014, 2016), 1 wt% of H_2O is the typical H_2O recorded within the melt inclusions at PdF for entrapment pressure of around 50 MPa (that is at the H_2O-CO_2 saturation pressure typically recorded by olivine hosted melt inclusions, which correspond to the main shallow magmatic system depth, around 2 km depth). This means that, since the main magmatic reservoir situated near the seal level, 0.4 wt% of the H_2O has been exsolved from the melt. In parallel, a simplified equation from La Spina et al. (2015) can be used to estimate the equivalent pressure (P, in Pa) of the different erupted component, using the dissolved H_2O content in the melt (x_d mass fraction) as well as the solubility coefficient (σ) and solubility exponent (ε): $x_d = \sigma(P)^{\varepsilon}$. Using the values reported in this last study, and the corresponding water content of the golden component (0.6 wt%), these calculations suggest that the equivalent pressure representative of the golden material is 6.5 MPa, equivalent to a depth of around 250 m. This pressure represent a minimum value of the magmatic reservoir pressure feeding the September 2016 eruption (this pressure can be higher as volatile exsolution may start at shallower depths compared to the magmatic reservoir depth). This interpretation is in agreement with the supposed presence of a multitude of relatively shallow reservoirs between the sea level and the surface (Michon et al., 2016).

The magmatic decompression rate of this eruption can be estimated thanks to the vesicle number density decompression rate meter of Toramaru (2006). Using a N_V of 9.0×10^3 mm^{-3}, we found an estimated decompression rate of 0.14 MPa s^{-1}, equivalent to a magmatic ascent rate of around 4 m s^{-1}. This value is consistent with typical decompression rates of basaltic eruptions (Ferguson et al., 2016; Shea, 2017) and similar to those calculated for the initial stages of the June 2014 eruption (0.15 MPa s^{-1}), but it is higher than the initial stage of the July 2015 eruption (0.08 MPa s^{-1}), which did not produce significant golden pumice and pre-eruptive nucleation (Thivet et al. submitted). Considering the estimated minimum depth of the magma reservoir and the decompression rate associated with the golden pumice material, the duration of the magma propagation from the reservoir to the surface should be at least 60 s.

Focusing on the CSD shapes, and considering the CSD theory (Higgins, 2000; Marsh, 1988), we were able to trace back the average growth (7.8×10^{-4} and 2.6×10^{-4} mm s^{-1} for plg and cpx microlites, respectively) and nucleation (15 and 9 mm^{-3} s^{-1} for plg and cpx microlites, respectively) rates of the golden component (Figure 11a; Table S5). These estimated values are in agreement with the ones found by the undercooling experiments of Arzilli, Morgavi, et al. (2019). These rates associated with relatively low residence time in the conduit leads to low microlites content, which maintain relatively low and typical basaltic magma viscosity of 1.4 10^2 Pa s estimated with the three-phase viscosity model (integrating the Maron & Pierce, 1956; Llewellin & Manga, 2005; Giordano et al., 2008; Mader et al., 2013 and Truby et al., 2015 models). Relatively high permeability has also been measured (Figure 7) within golden pumice and fluidal scoria (k_1 between 10^{-11} and 10^{-9} m^2) consistent with high gas percolation rate. APASH measurements indicate round-, vesicle-, and elongated-shapes ash particles (Figure 8a), which is consistent with low viscous magma, inertial fragmentation by rapid acceleration, and open-vent Hawaiian-style activity (Cashman & Scheu, 2015; Gonnerman & Manga 2014) all along the eruption within Vent A.

5.2.2. Sideromelane and Tachylite Scoria/Ash Emission as the Indicator of Rapid Change of the Subsurface Magmatic Conditions

The change of activity during the last day of the eruption is associated with a significant change of the deposit (i) grain sizes (Figure 3), (ii) particle textures (Figures 5, 6, 7, and 10) and (iii) shape (Figure 8). In this section, we investigate the origin of this unusual explosive dynamics of Vent B (gas or magma input, viscosity, permeability, and decompression rate), which was characterized by degassing, transient ash-dominated explosions, and bomb emissions (Figure 4). The sideromelane and tachylite ash emitted from Vent B is very different compared to the golden/fluidal ash and is characterized by a decrease in vesicle content (between 13 and 14 vol% for the sideromelane ash and between 7 and 10 vol% for the tachylite ash, depending on the methods used), by an increase in microlite (15 vol% and 100 vol%, respectively; Figure 10c) and by a differentiated matrix (Figure 9) with respect to the golden/fuidal component.

The slight CSD shift between the golden/fluidal ash and the sideromelane/tachylite ash (red arrow in Figure 11a) also show that the crystal content increase (Higgins, 2000) in this two latter components. The curved CSDs of the sideromelane and tachylite components also suggest that the steeper part of the CSD slopes of the relatively small microlites, compared to the linear CSDs of the golden/fluidal component, results from newly formed microlites at subsurface and degassed conditions associated with low time of crystallization and relatively high degree of undercooling. This is also causing the decrease of the crystal growth rates and the drastic increase in the nucleation rates (Figures 11a and 11b). On the other hand, we suggest that the slight more gentle CSD slopes for the biggest microlites are consistent with the progressive crystal growth (not obvious in terms of length but better visible with the width which not appears in the CSD plots) of the inherited golden/fluidal ash microlites (which form along the eruptive dyke during the magma degassing) that experienced an increase of the total duration of crystallization (Figure 11a). Therefore, this concave-upward shape of the CSD in the sideromelane and tachylite fragments can be interpreted as a mixing between different microlite populations generated during a complex magmatic history in which phases of crystallization took place under distinct and variable conditions as described for other volcanic systems (e.g., Armienti et al., 1994; Higgins, 2002, 2006; D'Oriano et al. 2014; Pompilio et al., 2017) and with petrological experiments (e.g., Marsh, 1988; Vona & Romano, 2013; Zieg & Lofgren, 2006). The CSD interpretation is supported by the difference in composition between the cores of the largest microlites ($An_{65\text{-}71}$ for plg and $Fs_{12\text{-}14}$ for cpx) and the small microlites compositions ($An_{56\text{-}64}$ for plg, $Fs_{12\text{-}17}$ for cpx). This indeed suggests that the largest microlites are inherited from an initial crystallization within the eruptive dyke and that the small microlites formed afterward near the surface with more sodic and ferric compositions

(secondary crystallization occurring before the fragmentation). Using the equation presented in the previous section, relating the dissolved water content in the sideromelane melt (0.05 wt%) and the pressure, we found an equivalent pressure representative of 0.1 MPa, which is coherent with the initial interpretation of the magmatic degassing and crystallization at ambient pressure.

Some melt temperatures measured from the sideromelane ash components are slightly higher than the golden/fluidal melt and bulk rock ones (1,124–1,121 °C). Regarding numerical models (La Spina et al., 2015), H_2O degassing should decrease the magma temperature. However, as shown by petrological experiments, H_2O degassing associated with the latent heat of crystallization should slightly increase the magma temperatures (Putirka, 2008).

In any case, the estimated decrease temperatures within the sideromelane ash (1,148 to 1,110 °C) support the idea of a progressive degassing and cooling-driven crystallization at the very shallow depth until the total crystallization of the magma associated with the appearance of ol microlites (Fo_{69-78}) and Fe-Ti-rich oxides in the tachylite component (<1,100 °C). Relatively low H_2O content in the melt, especially in the sideromelane component, shows that the explosive dynamics is not due to a gas-rich magma. Moreover, no sign of reheating features (sign of arrival of a hotter magma) is observed in all the eruptive products. The arrival/presence of the K_2O-rich magma did not add heat to the system, but the increase in lava flux was sufficient to pressurize it. The fact that the tachylite material can be either K_2O-poor (initial magma) or K_2O-rich (emitted since the 16) reflects that the tachylite material could start to form (by degassing and crystallization) shortly before 16 September, when K_2O-poor magma was still emitted and when Vent B started to decrease in terms of intensity and in which this dense tachylite material could accumulate.

In parallel, the progressive decrease of N_V (3.2×10^3 and 1.1×10^3 mm^{-3} for sideromelane and tachylite ash, respectively) and V_G/V_L ratio (0.2 for both sideromelane and tachylite ash; Figure 10a), as well as the low vesicle volumes and the bimodal vesicle population within the tachylite ash (Figure 10b), with respect to the golden/fluidal ash, suggest that the sideromelane and tachylite ash component result from the gas loss and bubble coalescence of the initial texture of the golden/fluidal component. Global decreases in porosity (Figure 6a) and in isolated vesicle content (Figure 6b) also highlight both gas loss and bubble coalescence. The absence of isolated vesicles in the tachylite lapilli-sized fragments also suggests that the tachylite scoria cooled progressively, in contrast to the golden and fluidal fragments that quenched faster in the air. We suggest that the progressive cooling favor the postfragmentation connections between the vesicles and the breaking of the solidified tachylite matrix (Colombier, Wadsworth, et al., 2017; Gurioli et al., 2018). Moreover, sideromelane and tachylite components are less porous and less permeable than the golden/fluidal one (Figure 7). Their Darcian permeabilities are measured down to 10^{-12} $m^{2,}$ showing a lower degree of gas percolation. Finally, APASH measurements show a progressive change of the ash morphology (Figures 8b and 8c): Sideromelane ash shape signature is approximately the same as the golden/fluidal one except that they no longer form elongated ash particles and Pele's hairs and tears, reflecting slight increase in magma viscosity (1.8×10^3 Pa s). Tachylite ash shape signature is very different from the two latter components, showing rough surfaces and reflecting drastic increase in viscosity (tends to 10^9 Pa s) and brittle fragmentation.

As a conclusion, we suggest that the sideromelane and tachylite textures are inherited from a progressive subsurface cooling, inducing advanced degassing and secondary crystallization of the magma, which may occur either by (i) recycling material within active vents as already proposed for Etna (D'Oriano et al., 2014) and/or (ii) by directly cooling of the magma at its free surface facilitated by the slight decrease in the lava flux (Figures 2a and 2b, clogging of Vent B) as already observed on Stromboli (Gurioli et al., 2014) and/or (iii) by collapse of inner parts of the vent as we observed some collapse and instabilities features within the eruptive vents (Figure 3) again observed at Stromboli (Capponi et al., 2016; Patrick et al., 2007). In each case, this degassed, crystallized, and viscous magma, represented by the sideromelane and mainly the tachylite component, formed a relatively impermeable magmatic layer at the fragmentation level within Vent B, during its decrease in activity mainly between 16 and 17 September. The suggested increase of lava flux during the last day of activity may have reactivated Vent B, which was at that moment clogged by this tachylite layer, in contrast with Vent A, which remained active in a sustained way. The fact that we observed some mingled scoria and ash between golden/fluidal or sideromelane magma, coating the tachylite material,

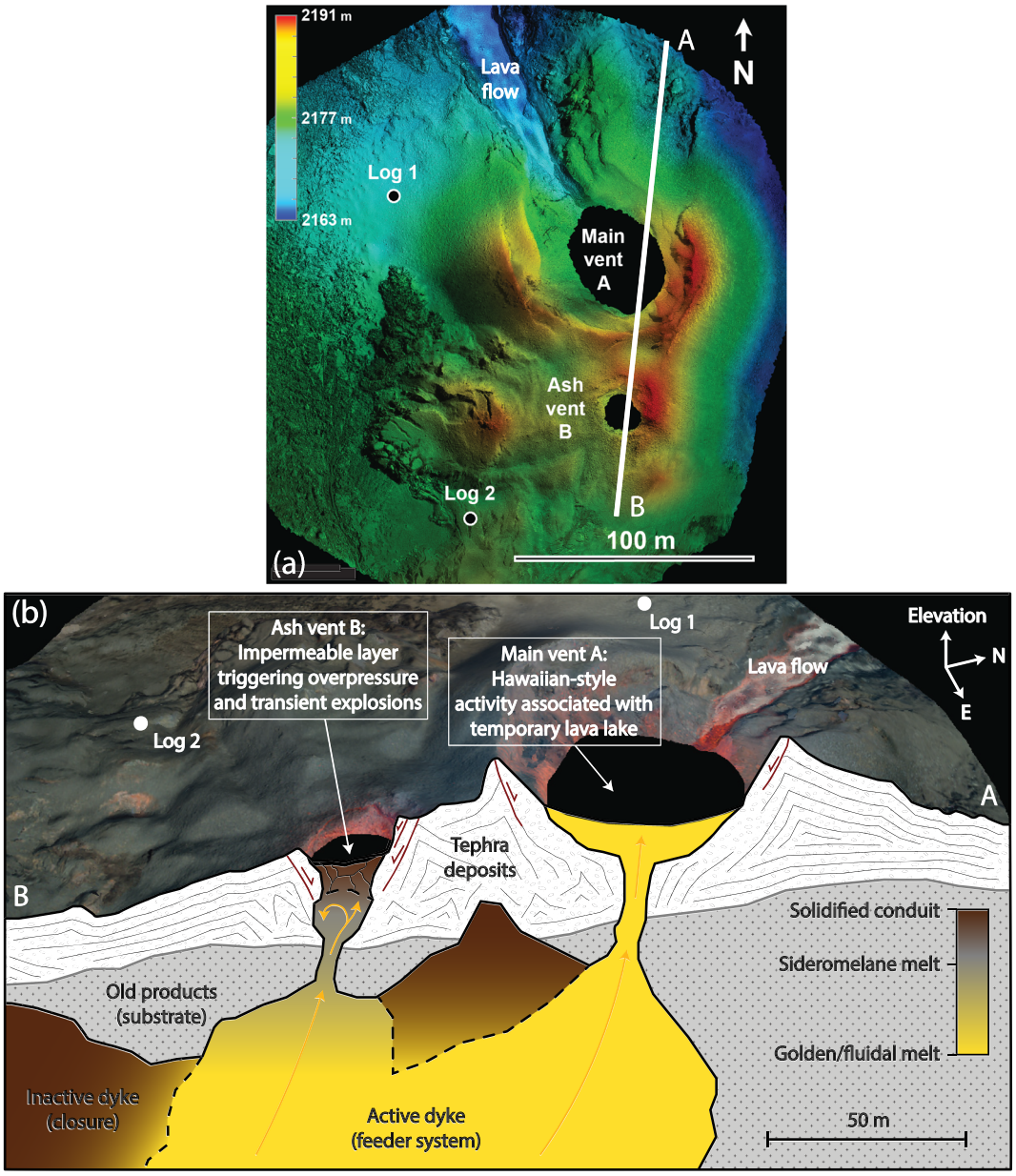

Figure 12. (a) DEM from aerial photogrammetry (15 September) of the main edifice of the eruption. (b) Schematic cross section showing the subsurface feeding system on 17 September.

confirms that the tachylite material is snatched and fragmented by the ascending and pressurized magma (secondary fragmentation), represented by the sideromelane and golden components, the last day of the eruption within Vent B.

Looking at field observations, slight degassing on the crater rim of Vent B during the last day of the eruption, as well as the source of the tachylite ash plume that also seemed to originate from the crater rim, suggests that some of the gas was able to escape. This released some pressure in the shallow system related to Vent B. However, we suppose that not all the gas was able to escape, resulting in an increase in the net pressure, which is equivalent to the pressure increase due to the ascending magma minus the slight decrease due to gas escape. Sudden and local pressure drops (caused by these initial overpressures that cracks the plug) would enhance further volatile exsolution and growth, promoting the magma fragmentation (La Spina et al., 2019).

6. Evidences of Plug Pressurization Triggering Relatively Energetic Fragmentation and Conclusions

Compared to several small eruptions of the 2014–2015 period documented by Peltier et al. (2016), Coppola et al. (2017), and Gurioli et al. (2018), the September 2016 eruption was characterized by relatively high lava fluxes which were associated with sustained, long-lasting lava fountaining producing a relative high amount of golden pumice. However, a significant, drastic and uncommon change of eruptive style was observed the last day of the eruption, only from the less active Vent B, while Vent A remained sustainably active with Hawaiian fountaining-dominated activity all along the eruption.

Regarding the eruption, we suggest that the stable lava flux between the 12 and 17 of September, followed by a drastic increase of intensity during the last day of the eruption, was an important parameter. Indeed, we suggest that the local magmatic flux emitted by Vent B, between the 16th and 17th, was insufficient to drain continuous magmatic flow in the subsurface eruptive conduit contrary to Vent A. This also highlights the importance of the subsurface conduit geometry evolution that may control the magma path at shallow levels (Pioli et al., 2017). This local magmatic flux decrease allowed the magma to degas and crystallize near the fragmentation/explosion level within Vent B (Figures 12a and 12b), forming a low-permeable and rheological plug whose fragmentation generated the tachylite material. Field observations, transitions between Hawaiian/Strombolian-style activities and transient explosions, and calculated crystal growth and nucleation rates suggest that this plug formed in approximately 1 or 2 days with averaged cooling rates between 0.005 and 0.05 °C s^{-1} (vs. 20 °C s^{-1} for a typical ash particle in the air, D'Oriano et al., 2014). This relatively slow plug cooling could have been caused by the combination of different processes as the direct cooling of the magma free-surface, and/or tephra recycling. The progressive clogging and burying of the Vent B might also been facilitate by the inner vent wall collapses (Gaudin et al., 2017).

Then, the late increase of the lava flux was enough to overcome the overpressure threshold to break through the plug layer and trigger the transient explosions within Vent B. Once the overpressure threshold required to let the magmatic gas percolate into the degassed plug was reached, the partially undegassed (golden/fluidal component) magma decompressed, then fragmented, and snatched some of the plug material (sideromelane and tachylite components and mingled material). Ash morphology measurements on tachylite ash, which represent the main ash emitted volume, show very different characteristics compare to the golden/fluidal ash. Tachylite ash is rounded in shape but with very rough particle surface, which is a characteristic of snatched and fragmented particles coming from a brittle material, reflecting secondary fragmentation (Cashman & Rust, 2016; Cashman & Scheu, 2015). This secondary fragmentation thus represents a hazardous mechanism producing a high amount of relatively fine particles with large dispersion, while the primary fragmentation within lava fountains (inertial fragmentation by rapid acceleration) produced smaller amount of golden and sideromelane ash. We also prove that combining geophysical, textural, and chemical measurements are critical to characterize, understand, and monitor such eruptive activity. In this study we also evidenced that this kind of approach allows to constrain relatively well the pre- and syn-eruptive processes at the origin of eruption dynamics.

Acknowledgments
We thank J-L. Devidal and J-M. Hénot for their valuable help for the use of the EPMA and the SEM, M. Benbakkar for the bulk rock analysis, measured at ICP-AES at the LMV. We also thank all the staff of the OVPF with whom we had constructive discussions. We thank the STRAP project funded by the Agence Nationale de la Recherche (ANR-14-CE03-0004-04) and the French government IDEX-ISITE initiative 16-IDEX-0001 (CAP 20-25). This research was financed by the French Government Laboratory of Excellence initiative ANR-10-LABX-0006, the Région Auvergne and the European Regional Development Fund. This is Laboratory of Excellence ClerVolc Contribution Number 391. This project has also received funding from the European Union's Horizon 2020 research and innovation programme under Grant Agreement 731070. Raw data and calculations used in this paper are available in the supporting information of this paper, in the public DynVolc repository data (https://doi.org/10.25519/DYNVOLC-Database), and in the EartChem library (URL: https://doi.org/10.1594/IEDA/111469) public domain repository complying with FAIR Data standards.

References

Andronico, D., Corsaro, R. A., Cristaldi, A., & Polacci, M. (2008). Characterizing high energy explosive eruptions at Stromboli volcano using multidisciplinary data: An example from the 9 January 2005 explosion. *Journal of Volcanology and Geothermal Research*, *176*(4), 541–550. https://doi.org/10.1016/j.jvolgeores.2008.05.011

Andronico, D., Lo Castro, M. D., Sciotto, M., & Spina, L. (2013). The 2010 ash emissions at the summit craters of Mt Etna: Relationship with seismo-acoustic signals. *Journal of Geophysical Research: Solid Earth*, *118*(1), 51–70. https://doi.org/10.1029/2012JB009895

Andronico, D., Cristaldi, A., Del Carlo, P., & Taddeucci, J. (2009). Shifting styles of basaltic explosive activity during the 2002-03 eruption of Mt. Etna, Italy. *Journal of Volcanology and Geothermal Research*, *180*(2–4), 110–122. https://doi.org/10.1016/j.jvolgeores.2008.07.026

Andronico, D., Scollo, S., Lo Castro, M. D., Cristaldi, A., Lodato, L., & Taddeucci, J. (2014). Eruption dynamics and tephra dispersal from the 24 November 2006 paroxysm at South-East Crater, Mt Etna, Italy. *Journal of Volcanology and Geothermal Research*, *274*, 78–91. https://doi.org/10.1016/j.jvolgeores.2014.01.009

Armienti, P., Pareschi, M. T., Innocenti, F., & Pompilio, M. (1994). Effects of magma storage and ascent on the kinetics of crystal growth. *Contributions to Mineralogy and Petrology*, *115*(4), 402–414. https://doi.org/10.1007/BF00320974

Arzilli, F., Agostini, C., Landi, P., Fortunati, A., Mancini, L., & Carroll, M. R. (2015). Plagioclase nucleation and growth kinetics in a hydrous basaltic melt by decompression experiments. *Contributions to Mineralogy and Petrology*, *170*(5–6), 1–16. https://doi.org/10.1007/s00410-015-1205-9

Arzilli, F., La Spina, G., Burton, M., Polacci, M., Le Gall, N., Hartley, M., & Nonni, S. (2019). Magma fragmentation in highly explosive basaltic eruptions induced by rapid crystallisation. *Nature Geoscience*, *12*(12), 1023–1028. https://doi.org/10.1038/s41561-019-0468-6

Arzilli, F., Morgavi, D., Petrelli, M., Polacci, M., Burton, M., Di Genova, D., et al. (2019). The unexpected explosive sub-Plinian eruption of Calbuco volcano (22–23 April 2015; southern Chile): Triggering mechanism implications. *Journal of Volcanology and Geothermal Research*, *378*, 35–50. https://doi.org/10.1016/j.jvolgeores.2019.04.006

Bai, L., Baker, D. R., & Hill, R. J. (2010). Permeability of vesicular Stromboli basaltic glass: Lattice Boltzmann simulations and laboratory measurements. *Journal of Geophysical Research*, *115*, B07201. https://doi.org/10.1029/2009JB007047

Bai, L., Baker, D. R., Polacci, M., & Hill, R. J. (2011). In-situ degassing study on crystal-bearing Stromboli basaltic magmas: Implications for Stromboli explosions. *Geophysical Research Letters*, *38*, L17309. https://doi.org/10.1029/2011GL048540

Barsotti, S., Andronico, D., Neri, A., Del Carlo, P., Baxter, P. J., Aspinall, W. P., & Hincks, T. (2010). Quantitative assessment of volcanic ash hazards for health and infrastructure at Mt. Etna (Italy) by numerical simulation. *Journal of Volcanology and Geothermal Research*, *192*(1–2), 85–96. https://doi.org/10.1016/j.jvolgeores.2010.02.011

Battaglia, J., Brenguier, F., & Roult, G. (2016). Seismic Monitoring at Piton de la Fournaise. *Active Volcanoes of the World*, (pp. 223–242). Berlin Heidelberg: Springer. https://doi.org/10.1007/978-3-642-31395-0_13

Blong, R. J. (1984). Hazards produced by volcanic eruptions. In *Volcanic Hazards*, (pp. 14–69). Sydney: Elsevier, Macquary University. https://doi.org/10.1016/B978-0-12-107180-6.50007-X

Blong, R. J. (1996). Volcanic hazards risk assessment. *Monitoring and Mitigation of Volcano Hazards*, (pp. 675–698). https://doi.org/10.1007/978-3-642-80087-0_20

Brown, S. K., Jenkins, S. F., Sparks, R. S. J., Odbert, H., & Auker, M. R. (2017). Volcanic fatalities database: Analysis of volcanic threat with distance and victim classification. *Journal of Applied Volcanology*, *6*(1), 1–20. https://doi.org/10.1186/s13617-017-0067-4

Burkhard, D. J. M. (2005). Nucleation and growth rates of pyroxene, plagioclase, and Fe-Ti oxides in basalt under atmospheric conditions. *European Journal of Mineralogy*, *17*(5), 675–686. https://doi.org/10.1127/0935-1221/2005/0017-0675

Burton, M., Allard, P., Mure, F., & La Spina, A. (2007). Magmatic gas composition reveals the source depth of slug-driven Strombolian explosive activity. *Science*, *317*(5835), 227–230. https://doi.org/10.1126/science.1141900

Büttner, R., Dellino, P., & Zimanowski, B. (1999). Identifying magma–water interaction from the surface features of ash particles. *Nature*, *401*(6754), 688–690. https://doi.org/10.1038/44364

Cannata, C. B., De Rosa, R., Donato, P., Donato, S., Lanzafame, G., Mancini, L., & Houghton, B. F. (2019). First 3D imaging characterization of Pele's hair from Kilauea volcano (Hawaii). *Scientific Reports*, *9*(1), 1711. https://doi.org/10.1038/s41598-018-37983-9

Capponi, A., Taddeucci, J., Scarlato, P., & Palladino, D. M. (2016). Recycled ejecta modulating Strombolian explosions. *Bulletin of Volcanology*, *78*(2), 1–13. https://doi.org/10.1007/s00445-016-1001-z

Carey, R. J., Manga, M., Degruyter, W., Swanson, D., Houghton, B., Orr, T., & Patrick, M. (2012). Externally triggered renewed bubble nucleation in basaltic magma: The 12 October 2008 eruption at Halemaumau Overlook vent, Klauea, Hawai'i, USA. *Journal of Geophysical Research*, *117*, B11202. https://doi.org/10.1029/2012JB009496

Cashman, K., & Rust, A. (2016). Introduction. In *Volcanic Ash*, (pp. 5–22). Bristol, United Kingdom: Elsevier, University of Bristol. https://doi.org/10.1016/B978-0-08-100405-0.00002-1

Cashman, K. V., & Scheu, B. (2015). Magmatic fragmentation. In *The Encyclopedia of Volcanoes*, (2nd ed.pp. 459–471). Narragansett, RI, USA: Elsevier, Graduate School of Oceanography, University of Rhode Island. https://doi.org/10.1016/B978-0-12-385938-9.00025-0

Cimarelli, C., Di Traglia, F., & Taddeucci, J. (2010). Basaltic scoria textures from a zoned conduit as precursors to violent Strombolian activity. *Geology*, *38*(5), 439–442. https://doi.org/10.1130/G30720.1

Cioni, R., D'Oriano, C., & Bertagnini, A. (2008). Fingerprinting ash deposits of small scale eruptions by their physical and textural features. *Journal of Volcanology and Geothermal Research*, *177*(1), 277–287. https://doi.org/10.1016/j.jvolgeores.2008.06.003

Cioni, R., Pistolesi, M., Bertagnini, A., Bonadonna, C., Hoskuldsson, A., & Scateni, B. (2014). Insights into the dynamics and evolution of the 2010 Eyjafjallajökull summit eruption (Iceland) provided by volcanic ash textures. *Earth and Planetary Science Letters*, *394*, 111–123. https://doi.org/10.1016/j.epsl.2014.02.051

Colò, L., Ripepe, M., Baker, D. R., & Polacci, M. (2010). Magma vesiculation and infrasonic activity at Stromboli open conduit volcano. *Earth and Planetary Science Letters*, *292*(3–4), 274–280. https://doi.org/10.1016/j.epsl.2010.01.018

Colombier, M., Gurioli, L., Druitt, T. H., Shea, T., Boivin, P., Miallier, D., & Cluzel, N. (2017). Textural evolution of magma during the 9.4-ka trachytic explosive eruption at Kilian Volcano, Chaîne des Puys, France. *Bulletin of Volcanology*, *79*(2), 17. https://doi.org/10.1007/s00445-017-1099-7

Colombier, M., Wadsworth, F. B., Gurioli, L., Scheu, B., Kueppers, U., Di Muro, A., & Dingwell, D. B. (2017). The evolution of pore connectivity in volcanic rocks. *Earth and Planetary Science Letters*, *462*, 99–109. https://doi.org/10.1016/j.epsl.2017.01.011

Coppola, D., & Cigolini, C. (2013). Thermal regimes and effusive trends at Nyamuragira volcano (DRC) from MODIS infrared data. *Bulletin of Volcanology*, *75*(8), 1–15. https://doi.org/10.1007/s00445-013-0744-z

Coppola, D., Di Muro, A., Peltier, A., Villeneuve, N., Ferrazzini, V., Favalli, M., et al. (2017). Shallow system rejuvenation and magma discharge trends at Piton de la Fournaise volcano (La Réunion Island). *Earth and Planetary Science Letters*, *463*(463), 13–24. https://doi.org/10.1016/j.epsl.2017.01.024

Coppola, D., Laiolo, M., Cigolini, C., Donne, D. D., & Ripepe, M. (2016). Enhanced volcanic hot-spot detection using MODIS IR data: Results from the MIROVA system. *Geological Society, London, Special Publications*, *426*(1), 181–205. https://doi.org/10.1144/SP426.5

Coppola, D., Piscopo, D., Staudacher, T., & Cigolini, C. (2009). Lava discharge rate and effusive pattern at Piton de la Fournaise from MODIS data. *Journal of Volcanology and Geothermal Research*, *184*(1–2), 174–192. https://doi.org/10.1016/j.jvolgeores.2008.11.031

Corsaro, R. A., Andronico, D., Behncke, B., Branca, S., Caltabiano, T., Ciancitto, F., et al. (2017). Monitoring the December 2015 summit eruptions of Mt. Etna (Italy): Implications on eruptive dynamics. *Journal of Volcanology and Geothermal Research*, *341*, 53–69. https://doi.org/10.1016/j.jvolgeores.2017.04.018

Costantini, L., Houghton, B. F., & Bonadonna, C. (2010). Constraints on eruption dynamics of basaltic explosive activity derived from chemical and microtextural study: The example of the Fontana Lapilli Plinian eruption, Nicaragua. *Journal of Volcanology and Geothermal Research*, *189*(3–4), 207–224. https://doi.org/10.1016/j.jvolgeores.2009.11.008

Dellino, P., Gudmundsson, M. T., Larsen, G., Mele, D., Stevenson, J. A., Thordarson, T., & Zimanowski, B. (2012). Ash from the Eyjafjallajökull eruption (Iceland): Fragmentation processes and aerodynamic behavior. *Journal of Geophysical Research*, *117*, B00C04. https://doi.org/10.1029/2011JB008726

Di Muro, A., Métrich, N., Allard, P., Aiuppa, A., Burton, M., Galle, B., & Staudacher, T. (2016). Magma Degassing at Piton de la Fournaise Volcano. In *Active Volcanoes of the Southwest Indian Ocean*, (pp. 203–222). Berlin Heidelberg: Springer. https://doi.org/10.1007/978-3-642-31395-0_12

Di Muro, A., Metrich, N., Vergani, D., Rosi, M., Armienti, P., Fougeroux, T., et al. (2014). The shallow plumbing system of Piton de la Fournaise Volcano (La Reunion Island, Indian Ocean) Revealed by the Major 2007 Caldera-Forming Eruption. *Journal of Petrology*, *55* (7), 1287–1315. https://doi.org/10.1093/petrology/egu025

Di Muro, A., Staudacher, T., Ferrazzini, V., Métrich, N., Besson, P., Garofalo, C., & Villemant, B. (2015). Shallow Magma Storage at Piton de la Fournaise Volcano After 2007 Summit Caldera Collapse Tracked in Pele's Hairs. In R. J. Carey, V. Cayol, M. P. Poland, & D. Weis (Eds.), *Hawaiian Volcanoes: From Source to Surface*, *American Geophysical Union Monograph*, (Vol. 208, pp. 189–212). Hoboken, New Jersey, États-Unis: John Wiley & Sons, Inc. https://doi.org/10.1002/9781118872079.ch9

Di Traglia, F., Cimarelli, C., de Rita, D., & Gimeno Torrente, D. (2009). Changing eruptive styles in basaltic explosive volcanism: Examples from Croscat complex scoria cone, Garrotxa Volcanic Field (NE Iberian Peninsula). *Journal of Volcanology and Geothermal Research*, *180*(2–4), 89–109. https://doi.org/10.1016/j.jvolgeores.2008.10.020

D'Oriano, C., Bertagnini, A., Cioni, R., & Pompilio, M. (2014). Identifying recycled ash in basaltic eruptions. *Scientific Reports*, *4*(1), 5851. https://doi.org/10.1038/srep05851

D'Oriano, C., Bertagnini, A., & Pompilio, M. (2011). Ash erupted during normal activity at Stromboli (Aeolian Islands, Italy) raises questions on how the feeding system works. *Bulletin of Volcanology*, *73*(5), 471–477. https://doi.org/10.1007/s00445-010-0425-0

DYNVOLC Database (2017). Observatoire de Physique du Globe de Clermont-Ferrand, Aubière, France, available at: https://doi.org/10.25519/DYNVOLC-Database.

Edwards, M. J., & Pioli, L. (2019). Magma and tephra characteristics for the 17–25 May 2016 Mt Etna eruption. *Data in Brief*, *22*, 65–71. https://doi.org/10.1016/j.dib.2018.11.093

Edwards, M. J., Pioli, L., Andronico, D., Scollo, S., Ferrari, F., & Cristaldi, A. (2018). Shallow factors controlling the explosivity of basaltic magmas: The 17–25 May 2016 eruption of Etna Volcano (Italy). *Journal of Volcanology and Geothermal Research*, *357*, 425–436. https://doi.org/10.1016/j.jvolgeores.2018.05.015

Eychenne, J., & Le Pennec, J.-L. (2012). Sigmoidal particle density distribution in a subplinian scoria fall deposit. *Bulletin of Volcanology*, *74*(10), 2243–2249. https://doi.org/10.1007/s00445-012-0671-4

Ferguson, D. J., Gonnermann, H. M., Ruprecht, P., Plank, T., Hauri, E. H., Houghton, B. F., & Swanson, D. A. (2016). Magma decompression rates during explosive eruptions of Kīlauea volcano, Hawaii, recorded by melt embayments. *Bulletin of Volcanology*, *78*(10), 1–12. https://doi.org/10.1007/s00445-016-1064-x

Formenti, Y., & Druitt, T. (2003). Vesicle connectivity in pyroclasts and implications for the fluidisation of fountain-collapse pyroclastic flows, Montserrat (West Indies). *Earth and Planetary Science Letters*, *214*(3–4), 561–574. https://doi.org/10.1016/S0012-821X(03)00386-8

Galle, B., Johansson, M., Rivera, C., Zhang, Y., Kihlman, M., Kern, C., et al. (2010). Network for Observation of Volcanic and Atmospheric Change (NOVAC)—A global network for volcanic gas monitoring: Network layout and instrument description. *Journal of Geophysical Research*, *115*, D05304. https://doi.org/10.1029/2009JD011823

Gaudin, D., Taddeucci, J., Scarlato, P., del Bello, E., Ricci, T., Orr, T., et al. (2017). Integrating puffing and explosions in a general scheme for Strombolian-style activity. *Journal of Geophysical Research: Solid Earth*, *122*(3), 1860–1875. https://doi.org/10.1002/2016JB013707

Giordano, D., Russell, J. K., & Dingwell, D. B. (2008). Viscosity of magmatic liquids: A model. *Earth and Planetary Science Letters*, *271*(1–4), 123–134. https://doi.org/10.1016/j.epsl.2008.03.038

Gonnermann, H. M., & Manga, M. (2014). Dynamics of magma ascent in the volcanic conduit. In T. K. P. Gregg, & R. M. C. Lopes (Eds.), *Modeling Volcanic Processes*, (Vol. 99, pp. 55–84). Cambridge: Cambridge University Press. https://doi.org/10.1017/CBO9781139021562.004

Gouhier, M., Guéhenneux, Y., Labazuy, P., Cacault, P., Decriem, J., & Rivet, S. (2016). HOTVOLC: a web-based monitoring system for volcanic hot spots. *Geological Society, London, Special Publications*, *426*(1), 223–241. https://doi.org/10.1144/SP426.31

Gouhier, M., Harris, A., Calvari, S., Labazuy, P., Guéhenneux, Y., Donnadieu, F., & Valade, S. (2012). Lava discharge during Etna's January 2011 fire fountain tracked using MSG-SEVIRI. *Bulletin of Volcanology*, *74*(4), 787–793. https://doi.org/10.1007/s00445-011-0572-y

Guéhenneux, Y., Gouhier, M., & Labazuy, P. (2015). Improved space borne detection of volcanic ash for real-time monitoring using 3-Band method. *Journal of Volcanology and Geothermal Research*, *293*, 25–45. https://doi.org/10.1016/j.jvolgeores.2015.01.005

Gurioli, L., Andronico, D., Bachelery, P., Balcone-Boissard, H., Battaglia, J., Boudon, G., et al. (2015). MeMoVolc consensual document: a review of cross-disciplinary approaches to characterizing small explosive magmatic eruptions. *Bulletin of Volcanology*, *77*(6), 1–33. https://doi.org/10.1007/s00445-015-0935-x

Gurioli, L., Colo', L., Bollasina, A. J., Harris, A. J. L., Whittington, A., & Ripepe, M. (2014). Dynamics of Strombolian explosions: Inferences from field and laboratory studies of erupted bombs from Stromboli volcano. *Journal of Geophysical Research: Solid Earth*, *119*(1), 319–345. https://doi.org/10.1002/2013JB010355

Gurioli, L., Di Muro, A., Vlastélic, I., Moune, S., Thivet, S., Valer, M., et al. (2018). Integrating field, textural, and geochemical monitoring to track eruption triggers and dynamics: a case study from Piton de la Fournaise. *Solid Earth*, *9*(2), 431–455. https://doi.org/10.5194/se-9-431-2018

Gurioli, L., Harris, A. J. L., Colò, L., Bernard, J., Favalli, M., Ripepe, M., & Andronico, D. (2013). Classification, landing distribution, and associated flight parameters for a bomb field emplaced during a single major explosion at Stromboli, Italy. *Geology*, *41*(5), 559–562. https://doi.org/10.1130/G33967.1

Gurioli, L., Harris, A. J. L., Houghton, B. F., Polacci, M., & Ripepe, M. (2008). Textural and geophysical characterization of explosive basaltic activity at Villarrica volcano. *Journal of Geophysical Research*, *113*, B08206. https://doi.org/10.1029/2007JB005328

Harris, A. J. L., Villeneuve, N., Di Muro, A., Ferrazzini, V., Peltier, A., Coppola, D., et al. (2017). Effusive crises at Piton de la Fournaise 2014–2015: A review of a multi-national response model. *Journal of Applied Volcanology*, *6*(1), 1, 11–29. https://doi.org/10.1186/s13617-017-0062-9

Heiken, G. (1974). Atlas of volcanic ash. *Smithsonian Contributions to the Earth Sciences*, *12*(12), 1–101. https://doi.org/10.5479/si.00810274.12.1

Hibert, C., Mangeney, A., Polacci, M., Di Muro, A., Vergniolle, S., Ferrazzini, V., et al. (2015). Toward continuous quantification of lava extrusion rate: Results from the multidisciplinary analysis of the 2 January 2010 eruption of Piton de la Fournaise volcano, La Réunion. *Journal of Geophysical Research: Solid Earth*, *120*(5), 3026–3047. https://doi.org/10.1002/2014JB011769

Higgins, M. D. (2000). Measurement of crystal size distributions. *American Mineralogist*, *85*(9), 1105–1116. https://doi.org/10.2138/am-2000-8-901

Higgins, M. D. (2002). Closure in crystal size distributions (CSD), verification of CSD calculations, and the significance of CSD fans. *American Mineralogist*, *87*(1), 171–175. https://doi.org/10.2138/am-2002-0118

Higgins, M. D. (2006). *Quantitative textural measurements in igneous and metamorphic petrology*. Cambridge: Cambridge University Press. https://doi.org/10.1017/CBO9780511535574

Holt, S. J., Carey, R. J., Houghton, B. F., Orr, T., McPhie, J., & Feig, S. (2019). Eruption and fountaining dynamics of selected 1985–1986 high fountaining episodes at Kīlauea volcano, Hawai'i, from quantitative vesicle microtexture analysis. *Journal of Volcanology and Geothermal Research*, *369*, 21–34. https://doi.org/10.1016/j.jvolgeores.2018.11.011

Houghton, B. F., Taddeucci, J., Andronico, D., Gonnermann, H. M., Pistolesi, M., Patrick, M. R., et al. (2016). Stronger or longer: Discriminating between Hawaiian and Strombolian eruption styles. *Geology*, *44*(2), 163–166. https://doi.org/10.1130/G37423.1

Houghton, B. F., & Wilson, C. J. N. (1989). A vesicularity index for pyroclastic deposits. *Bulletin of Volcanology*, *51*(6), 451–462. https://doi.org/10.1007/BF01078811

Houghton, B. F., Wilson, C. J. N., Del Carlo, P., Coltelli, M., Sable, J. E., & Carey, R. (2004). The influence of conduit processes on changes in style of basaltic Plinian eruptions: Tarawera 1886 and Etna 122 BC. *Journal of Volcanology and Geothermal Research*, *137*(1–3), 1–14. https://doi.org/10.1016/j.jvolgeores.2004.05.009

Jones, T. J., Houghton, B. F., Llewellin, E. W., Parcheta, C. E., & Höltgen, L. (2018). Spatter matters—Distinguishing primary (eruptive) and secondary (non-eruptive) spatter deposits. *Scientific Reports*, *8*(1), 9179. https://doi.org/10.1038/s41598-018-27065-1

Kawabata, E., Cronin, S. J., Bebbington, M. S., Moufti, M. R. H., El-Masry, N., & Wang, T. (2015). Identifying multiple eruption phases from a compound tephra blanket: An example of the AD1256 Al-Madinah eruption, Saudi Arabia. *Bulletin of Volcanology*, *77*(1), 6. https://doi.org/10.1007/s00445-014-0890-y

La Spina, G., Burton, M., & de' Michieli Vitturi, M. (2015). Temperature evolution during magma ascent in basaltic effusive eruptions: A numerical application to Stromboli volcano. *Earth and Planetary Science Letters*, *426*, 89–100. https://doi.org/10.1016/j.epsl.2015.06.015

La Spina, G., Clarke, A. B., de' Michieli Vitturi, M., Burton, M., Allison, C. M., Roggensack, K., & Alfano, F. (2019). Conduit dynamics of highly explosive basaltic eruptions: The 1085 CE Sunset Crater sub-Plinian events. *Journal of Volcanology and Geothermal Research*, *387*, 106658. https://doi.org/10.1016/j.jvolgeores.2019.08.001

Lange, R. A., Frey, H. M., & Hector, J. (2009). A thermodynamic model for the plagioclase-liquid hygrometer/thermometer. *American Mineralogist*, *94*(4), 494–506. https://doi.org/10.2138/am.2009.3011

Lautze, N., Taddeucci, J., Andronico, D., Houghton, B., Niemeijer, A., & Scarlato, P. (2013). Insights into explosion dynamics and the production of ash at Stromboli from samples collected in real-time, October 2009. *Special Paper of the Geological Society of America*, *498*, 125–139. https://doi.org/10.1130/2013.2498(08)

Lautze, N. C., & Houghton, B. F. (2005). Physical mingling of magma and complex eruption dynamics in the shallow conduit at Stromboli volcano, Italy. *Geology*, *33*(5), 425–428. https://doi.org/10.1130/G21325.1

Lautze, N. C., Taddeucci, J., Andronico, D., Cannata, C., Tornetta, L., Scarlato, P., et al. (2012). SEM-based methods for the analysis of basaltic ash from weak explosive activity at Etna in 2006 and the 2007 eruptive crisis at Stromboli. *Physics and Chemistry of the Earth*, *45-46*, 113–127. https://doi.org/10.1016/j.pce.2011.02.001

Leduc, L., Gurioli, L., Harris, A., Colò, L., & Rose-Koga, E. F. (2015). Types and mechanisms of strombolian explosions: Characterization of a gas-dominated explosion at Stromboli. *Bulletin of Volcanology*, *77*(1), 1–15. https://doi.org/10.1007/s00445-014-0888-5

Leibrandt, S., & Le Pennec, J.-L. (2015). Towards fast and routine analyses of volcanic ash morphometry for eruption surveillance applications. *Journal of Volcanology and Geothermal Research*, *297*, 11–27. https://doi.org/10.1016/j.jvolgeores.2015.03.014

Liu, E. J., Cashman, K. V., & Rust, A. C. (2015). Optimising shape analysis to quantify volcanic ash morphology. *GeoResJ*, *8*, 14–30. https://doi.org/10.1016/j.grj.2015.09.001

Llewellin, E. W., & Manga, M. (2005). Bubble suspension rheology and implications for conduit flow. *Journal of Volcanology and Geothermal Research*, *143*(1–3), 205–217. https://doi.org/10.1016/j.jvolgeores.2004.09.018

Mader, H. M., Llewellin, E. W., & Mueller, S. P. (2013). The rheology of two-phase magmas: A review and analysis. *Journal of Volcanology and Geothermal Research*, *257*, 135–158. https://doi.org/10.1016/j.jvolgeores.2013.02.014

Mangan, M. T., & Cashman, K. V. (1996). The structure of basaltic scoria and reticulite and inferences for vesiculation, foam formation, and fragmentation in lava fountains. *Journal of Volcanology and Geothermal Research*, *73*(1–2), 1–18. https://doi.org/10.1016/0377-0273(96)00018-2

Maria, A., & Carey, S. (2007). Quantitative discrimination of magma fragmentation and pyroclastic transport processes using the fractal spectrum technique. *Journal of Volcanology and Geothermal Research*, *161*(3), 234–246. https://doi.org/10.1016/j.jvolgeores.2006.12.006

Maron, S. H., & Pierce, P. E. (1956). Application of ree-eyring generalized flow theory to suspensions of spherical particles. *Journal of Colloid Science*, *11*(1), 80–95. https://doi.org/10.1016/0095-8522(56)90023-X

Marsh, B. D. (1988). Crystal size distribution (CSD) in rocks and the kinetics and dynamics of crystallization. *Contributions to Mineralogy and Petrology*, *99*(3), 277–291. https://doi.org/10.1007/BF00375362

Michon, L., Di Muro, A., Villeneuve, N., Saint-Marc, C., Fadda, P., & Manta, F. (2013). Explosive activity of the summit cone of Piton de la Fournaise volcano (La Réunion island): A historical and geological review. *Journal of Volcanology and Geothermal Research*, *264*, 117–133. https://doi.org/10.1016/j.jvolgeores.2013.06.012

Michon, L., Ferrazzini, V., & Di Muro, A. (2016). Magma paths at Piton de la Fournaise volcano. *Active Volcanoes of the Southwest Indian Ocean*, 91–106. https://doi.org/10.1007/978-3-642-31395-0

Miwa, T., & Toramaru, A. (2013). Conduit process in vulcanian eruptions at Sakurajima volcano, Japan: Inference from comparison of volcanic ash with pressure wave and seismic data. *Bulletin of Volcanology*, *75*(1), 1–13. https://doi.org/10.1007/s00445-012-0685-y

Miwa, T., Toramaru, A., & Iguchi, M. (2009). Correlations of volcanic ash texture with explosion earthquakes from vulcanian eruptions at Sakurajima volcano, Japan. *Journal of Volcanology and Geothermal Research*, *184*(3–4), 473–486. https://doi.org/10.1016/j.jvolgeores.2009.05.012

Morandi, A., Di Muro, A., Principe, C., Michon, L., Leroi, G., Norelli, F., & Bachelery, P. (2016). Pre-historic (<5 kiloyear) Explosive Activity at Piton de la Fournaise Volcano. *Active Volcanoes of the Southwest Indian Ocean*, 107–138. https://doi.org/10.1007/978-3-642-31395-0

Morgan, D. J., & Jerram, D. A. (2006). On estimating crystal shape for crystal size distribution analysis. *Journal of Volcanology and Geothermal Research*, *154*(1–2), 1–7. https://doi.org/10.1016/j.jvolgeores.2005.09.016

Morin, J., Bachèlery, P., Soulé, H., & Nassor, H. (2016). Volcanic risk and crisis management on Grande Comore Island. In *Active Volcanoes of the Southwest Indian Ocean. Active Volcanoes of the World*, (Vol. 4, pp. 403–422). Berlin Heidelberg: Springer. https://doi.org/10.1007/978-3-642-31395-0_25

Nurfiani, D., & Bouvet de Maisonneuve, C. (2018). Furthering the investigation of eruption styles through quantitative shape analyses of volcanic ash particles. *Journal of Volcanology and Geothermal Research*, *354*, 102–114. https://doi.org/10.1016/j.jvolgeores.2017.12.001

Ort, M. H., Di Muro, A., Michon, L., & Bachèlery, P. (2016). Explosive eruptions from the interaction of magmatic and hydrothermal systems during flank extension: The Bellecombe Tephra of Piton de La Fournaise (La Réunion Island). *Bulletin of Volcanology*, *78*(1), 1–14. https://doi.org/10.1007/s00445-015-0998-8

Papale, P. (2017). Rational volcanic hazard forecasts and the use of volcanic alert levels. *Journal of Applied Volcanology*, *6*(1), 1–13. https://doi.org/10.1186/s13617-017-0064-7

Parcheta, C. E., Houghton, B. F., & Swanson, D. A. (2013). Contrasting patterns of vesiculation in low, intermediate, and high Hawaiian fountains: A case study of the 1969 Mauna Ulu eruption. *Journal of Volcanology and Geothermal Research*, *255*, 79–89. https://doi.org/10.1016/j.jvolgeores.2013.01.016

Patrick, M. R., Harris, A. J. L., Ripepe, M., Dehn, J., Rothery, D. A., & Calvari, S. (2007). Strombolian explosive styles and source conditions: insights from thermal (FLIR) video. *Bulletin of Volcanology*, *69*(7), 769–784. https://doi.org/10.1007/s00445-006-0107-0

Peltier, A., Beauducel, F., Villeneuve, N., Ferrazzini, V., Di Muro, A., Aiuppa, A., et al. (2016). Deep fluid transfer evidenced by surface deformation during the 2014–2015 unrest at Piton de la Fournaise volcano. *Journal of Volcanology and Geothermal Research*, *321*, 140–148. https://doi.org/10.1016/j.jvolgeores.2016.04.031

Peltier, A., Staudacher, T., Bachèlery, P., & Cayol, V. (2009). Formation of the April 2007 caldera collapse at Piton de La Fournaise volcano: Insights from GPS data. *Journal of Volcanology and Geothermal Research*, *184*(1–2), 152–163. https://doi.org/10.1016/j.jvolgeores.2008.09.009

Peltier, A., Villeneuve, N., Ferrazzini, V., Testud, S., Hassen Ali, T., Boissier, P., & Catherine, P. (2018). Changes in the long-term geophysical eruptive precursors at Piton de la Fournaise: Implications for the response management. *Frontiers in Earth Science*, *6*(July), 1–10. https://doi.org/10.3389/feart.2018.00104

Pichavant, M., Brugier, Y., & Di Muro, A. (2016). Petrological and experimental constraints on the evolution of Piton de la Fournaise magmas. In *Active Volcanoes of the Southwest Indian Ocean*, (pp. 171–184). Berlin Heidelberg: Springer. https://doi.org/10.1007/978-3-642-31395-0_10

Pioli, L., Azzopardi, B. J., Bonadonna, C., Brunet, M., & Kurokawa, A. K. (2017). Outgassing and eruption of basaltic magmas: The effect of conduit geometry. *Geology*, *45*(8), G38787.1. https://doi.org/10.1130/G38787.1

Pioli, L., Pistolesi, M., & Rosi, M. (2014). Transient explosions at open-vent volcanoes: The case of Stromboli (Italy). *Geology*, *42*(10), 863–866. https://doi.org/10.1130/G35844.1

Pistolesi, M., Donne, D. D., Pioli, L., Rosi, M., & Ripepe, M. (2011). The 15 March 2007 explosive crisis at Stromboli volcano, Italy: Assessing physical parameters through a multidisciplinary approach. *Journal of Geophysical Research*, *116*, B12206. https://doi.org/10.1029/2011JB008527

Polacci, M., Burton, M. R., La Spina, A., Murè, F., Favretto, S., & Zanini, F. (2009). The role of syn-eruptive vesiculation on explosive basaltic activity at Mt. Etna, Italy. *Journal of Volcanology and Geothermal Research*, *179*(3–4), 265–269. https://doi.org/10.1016/j.jvolgeores.2008.11.026

Polacci, M., Corsaro, R. A., & Andronico, D. (2006). Coupled textural and compositional characterization of basaltic scoria: Insights into the transition from Strombolian to fire fountain activity at Mount Etna, Italy. *Geology*, *34*(3), 201. https://doi.org/10.1130/G22318.1

Pompilio, M., Bertagnini, A., Del Carlo, P., & Di Roberto, A. (2017). Magma dynamics within a basaltic conduit revealed by textural and compositional features of erupted ash: the December 2015 Mt. Etna paroxysms. *Scientific Reports*, *7*(1), 4805. https://doi.org/10.1038/s41598-017-05065-x

Porritt, L. A., Russell, J. K., & Quane, S. L. (2012). Pele's tears and spheres: Examples from Kilauea Iki. *Earth and Planetary Science Letters*, *333–334*, 171–180. https://doi.org/10.1016/j.epsl.2012.03.031

Potuzak, M., Nichols, A. R. L., Dingwell, D. B., & Clague, D. A. (2008). Hyperquenched volcanic glass from Loihi Seamount, Hawaii. *Earth and Planetary Science Letters*, *270*(1–2), 54–62. https://doi.org/10.1016/j.epsl.2008.03.018

Principe, C., Morandi, A., Di Muro, A., & Michon, L. (2016). Volcanological map of the Plaine des Sables, Piton de la Fournaise. In *Active Volcanoes of the Southwest Indian Ocean. Active Volcanoes of the World*, (pp. 327–330). Berlin Heidelberg: Springer. https://doi.org/10.1007/978-3-642-31395-0_20

Putirka, K. D. (2008). Thermometers and barometers for volcanic systems. *Reviews in Mineralogy and Geochemistry*, *69*(1), 61–120. https://doi.org/10.2138/rmg.2008.69.3

Riley, C. M., Rose, W. I., & Bluth, G. J. S. (2003). Quantitative shape measurements of distal volcanic ash. *Journal of Geophysical Research*, *108*(B10), 2504. https://doi.org/10.1029/2001JB000818

Romero, J. E., Vera, F., Polacci, M., Morgavi, D., Arzilli, F., Alam, M. A., et al. (2018). Tephra from the 3 March 2015 sustained column related to explosive lava fountain activity at Volcán Villarrica (Chile). *Frontiers in Earth Science*, *6*. https://doi.org/10.3389/feart.2018.00098

Rosseel, J. B., White, J. D. L., & Houghton, B. F. (2006). Complex bombs of phreatomagmatic eruptions: Role of agglomeration and welding in vents of the 1886 Rotomahana eruption, Tarawera, New Zealand. *Journal of Geophysical Research*, *111*, B12205. https://doi.org/10.1029/2005JB004073

Roult, G., Peltier, A., Taisne, B., Staudacher, T., Ferrazzini, V., & Di Muro, A. (2012). A new comprehensive classification of the Piton de la Fournaise activity spanning the 1985–2010 period. Search and analysis of short-term precursors from a broad-band seismological station. *Journal of Volcanology and Geothermal Research*, *241-242*, 78–104. doi:https://doi.org/10.1016/j.jvolgeores.2012.06.012

Rust, A. C., & Cashman, K. V. (2004). Permeability of vesicular silicic magma: Inertial and hysteresis effects. *Earth and Planetary Science Letters*, *228*(1–2), 93–107. https://doi.org/10.1016/j.epsl.2004.09.025

Sable, J. E., Houghton, B. F., Del Carlo, P., & Coltelli, M. (2006). Changing conditions of magma ascent and fragmentation during the Etna 122 BC basaltic Plinian eruption: Evidence from clast microtextures. *Journal of Volcanology and Geothermal Research*, *158*(3–4), 333–354. https://doi.org/10.1016/j.jvolgeores.2006.07.006

Schmith, J., Höskuldsson, Á., & Holm, P. M. (2017). Grain shape of basaltic ash populations: Implications for fragmentation. *Bulletin of Volcanology*, *79*(2), 1–16. https://doi.org/10.1007/s00445-016-1093-5

Scollo, S., Coltelli, M., Bonadonna, C., & Del Carlo, P. (2013). Tephra hazard assessment at Mt. Etna (Italy). *Natural Hazards and Earth System Sciences*, *13*(12), 3221–3233. https://doi.org/10.5194/nhess-13-3221-2013

Shea, T. (2017). Bubble nucleation in magmas: A dominantly heterogeneous process? *Journal of Volcanology and Geothermal Research*, *343*, 155–170. https://doi.org/10.1016/j.jvolgeores.2017.06.025

Shea, T., Houghton, B. F., Gurioli, L., Cashman, K. V., Hammer, J. E., & Hobden, B. J. (2010). Textural studies of vesicles in volcanic rocks: An integrated methodology. *Journal of Volcanology and Geothermal Research*, *190*(3–4), 271–289. https://doi.org/10.1016/j.jvolgeores.2009.12.003

Sheridan, M. F., & Marshall, J. R. (1983). Interpretation of pyroclast surface features using sem images. *Journal of Volcanology and Geothermal Research*, *16*(1–2), 153–159. https://doi.org/10.1016/0377-0273(83)90088-4

Sparks, R. S. J. (1978). The dynamics of bubble formation and growth in magmas: A review and analysis. *Journal of Volcanology and Geothermal Research*, *3*(1–2), 1–37. https://doi.org/10.1016/0377-0273(78)90002-1

Staudacher, T., Ferrazzini, V., Peltier, A., Kowalski, P., Boissier, P., Catherine, P., et al. (2009). The April 2007 eruption and the Dolomieu crater collapse, two major events at Piton de la Fournaise (La Réunion Island, Indian Ocean). *Journal of Volcanology and Geothermal Research*, *184*(1–2), 126–137. https://doi.org/10.1016/j.jvolgeores.2008.11.005

Staudacher, T., Peltier, A., Ferrazzini, V., Di Muro, A., Boissier, P., Catherine, P., et al. (2016). Fifteen years of intense eruptive activity (1998-2013) at Piton de la Fournaise volcano: a review. In *Active Volcanoes of the Southwest Indian Ocean*, (pp. 139–170). Berlin Heidelberg: Springer. https://doi.org/10.1007/978-3-642-31395-0_9

Stovall, W. K., Houghton, B. F., Gonnermann, H., Fagents, S. A., & Swanson, D. A. (2011). Eruption dynamics of Hawaiian-style fountains: The case study of episode 1 of the Kīlauea Iki 1959 eruption. *Bulletin of Volcanology*, *73*(5), 511–529. https://doi.org/10.1007/s00445-010-0426-z

Stovall, W. K., Houghton, B. F., Hammer, J. E., Fagents, S. A., & Swanson, D. A. (2012). Vesiculation of high fountaining Hawaiian eruptions: Episodes 15 and 16 of 1959 Kīlauea Iki. *Bulletin of Volcanology*, *74*(2), 441–455. https://doi.org/10.1007/s00445-011-0531-7

Taddeucci, J., Pompilio, M., & Scarlato, P. (2004). Conduit processes during the July–August 2001 explosive activity of Mt. Etna (Italy): Inferences from glass chemistry and crystal size distribution of ash particles. *Journal of Volcanology and Geothermal Research*, *137*(1–3), 33–54. https://doi.org/10.1016/j.jvolgeores.2004.05.011

Taddeucci, J., Pompilio, M., & Scarlato, P. (2002). Monitoring the explosive activity of the July-August 2001 eruption of Mt. Etna (Italy) by ash characterization. *Geophysical Research Letters*, *29*(8), 1230. https://doi.org/10.1029/2001GL014372

Takeuchi, S., Nakashima, S., & Tomiya, A. (2008). Permeability measurements of natural and experimental volcanic materials with a simple permeameter: Toward an understanding of magmatic degassing processes. *Journal of Volcanology and Geothermal Research*, *177*(2), 329–339. https://doi.org/10.1016/j.jvolgeores.2008.05.010

Toramaru, A. (2006). BND (bubble number density) decompression rate meter for explosive volcanic eruptions. *Journal of Volcanology and Geothermal Research*, *154*(3–4), 303–316. https://doi.org/10.1016/j.jvolgeores.2006.03.027

Toramaru, A. (1989). Vesiculation process and bubble size distributions in ascending magmas with constant velocities. *Journal of Geophysical Research*, *94*(B12), 17523. https://doi.org/10.1029/JB094iB12p17523

Truby, J. M., Mueller, S. P., Llewellin, E. W., & Mader, H. M. (2015). The rheology of three-phase suspensions at low bubble capillary number. *Proceedings of the Royal Society A: Mathematical, Physical and Engineering Sciences*, *471*(2173), 20140557. https://doi.org/10.1098/rspa.2014.0557

Villemant, B., Salaün, A., & Staudacher, T. (2009). Evidence for a homogeneous primary magma at Piton de la Fournaise (La Réunion): A geochemical study of matrix glass, melt inclusions and Pélé's hairs of the 1998-2008 eruptive activity. *Journal of Volcanology and Geothermal Research*, *184*(1–2), 79–92. https://doi.org/10.1016/j.jvolgeores.2009.03.015

Vlastélic, I., Gannoun, A., Di Muro, A., Gurioli, L., Bachèlery, P., & Henot, J. M. (2016). Origin and fate of sulfide liquids in hotspot volcanism (La Réunion): Pb isotope constraints from residual Fe–Cu oxides. *Geochimica et Cosmochimica Acta*, *194*, 179–192. https://doi.org/10.1016/j.gca.2016.08.036

Vona, A., & Romano, C. (2013). The effects of undercooling and deformation rates on the crystallization kinetics of Stromboli and Etna basalts. *Contributions to Mineralogy and Petrology*, *166*(2), 491–509. https://doi.org/10.1007/s00410-013-0887-0

Walker, G. P. L., & Croasdale, R. (1971). Characteristics of some basaltic pyroclastics. *Bulletin Volcanologique*, *35*(2), 303–317. https://doi.org/10.1007/BF02596957

White, J. D. L., & Houghton, B. F. (2006). Primary volcaniclastic rocks. *Geology*, *34*(8), 677. https://doi.org/10.1130/G22346.1

Wohletz, K. H. (1983). Mechanisms of hydrovolcanic pyroclast formation: Grain-size, scanning electron microscopy, and experimental studies. *Journal of Volcanology and Geothermal Research*, *17*(1–4), 31–63. https://doi.org/10.1016/0377-0273(83)90061-6

Xu, Z., & Zhang, Y. (2002). Quench rates in air, water, and liquid nitrogen, and inference of temperature in volcanic eruption columns. *Earth and Planetary Science Letters*, *200*(3–4), 315–330. https://doi.org/10.1016/S0012-821X(02)00656-8

Zieg, M. J., & Lofgren, G. E. (2006). An experimental investigation of texture evolution during continuous cooling. *Journal of Volcanology and Geothermal Research*, *154*(1–2), 74–88. https://doi.org/10.1016/j.jvolgeores.2005.09.020